Near-surface soil heat flux and evaporation dynamics using heat pulse probes

by

Sudipti Parajuli

B.Sc., Tribhuvan University, 2018

A THESIS

submitted in partial fulfillment of the requirements for the degree

MASTER OF SCIENCE

Department of Agronomy
College of Agriculture

KANSAS STATE UNIVERSITY
Manhattan, Kansas

2025

Approved by:

Major Professor
Eduardo Alvarez Santos

Copyright

Abstract

Evaporation is an important component of the soil water balance. Accurate and dynamic measurements of evaporation are important to identify water management practices that minimize evaporation losses and increase agricultural productivity. Most of the existing methods for quantifying soil evaporation do not provide depth-resolved information on near-surface evaporation dynamics. This thesis explores the potential of applying the sensible heat balance (SHB) method to quantify the temporal and spatial patterns of sub-surface evaporation using field-based experiments. The first chapter of this thesis focuses on determining soil thermal properties and heat balance components using three-needle heat pulse probes. The study investigates the prospects of heat pulse probes in determining near-surface soil heat flux and heat storage using millimeter-scale measurements of soil temperature and thermal properties. The second chapter examines the performance of the sensible heat balance method to estimate near-surface soil evaporation by comparing it with evaporation measurements from the Eddy Covariance (EC) and microlysimeter methods. Temporal and spatial analysis of soil sensible heat flux demonstrated that heat flux densities decreased in magnitude with depth, and temperature gradient was the major factor influencing heat flux. Change in soil sensible heat storage showed lower values at all depths as compared to heat flux. Good agreement (R^2 = 0.62) was observed between evaporation from the SHB and EC methods, whereas no correlation was seen between evaporation estimates from the SHB and microlysimeter methods. Overall, our findings show the potential of the SHB method for fine time (30 min) and depth (mm) scale measurements of evaporation.

Table of Contents

List of Figures

Acknowledgements

I am profoundly grateful to everyone who has contributed to shaping my academic journey in a myriad of ways. I owe a special debt of gratitude to my major advisor, Dr. Eduardo Santos, for granting me this incredible opportunity and placing his trust in me. Without his guidance, encouragement, and relentless support, this work may not have concluded this way. I sincerely appreciate my committee members, Dr. Gerard Kluitenberg and Dr. Andres Patrignani, for their insightful suggestions and continuous guidance throughout the process. I also thank Justin Knopf and Manhattan Plant Materials Center (KSPMC) for allowing to carry out this research in their field plot.

To my family - my father, mother, and sister - thank you for being my greatest supporters. Your unwavering encouragement means the world to me, and I am forever grateful. A heartfelt thank you to my husband for his love, support, encouragement, and, above all, his infinite patience.

Lastly, I extend my warmest appreciation to my friends and colleagues for their kindness and support. Your presence has made this journey even more fulfilling.

Chapter 1 - General Introduction

1.1 Evapotranspiration

The soil water balance represents the movement and distribution of water across the land surface, with precipitation as the primary inflow and evapotranspiration, canopy interception, surface and sub-surface runoff, and drainage as the main outflow components. The relative proportions of these individual components determine the water budget of a region (Wilcox et al., 2003). Evapotranspiration (*ET*), the combined process of plant transpiration (*T*) and soil evaporation (*E*), is important for various applications, including plant-growth modeling, irrigation and water management, climate change studies, plant physiology and agronomy studies assessing the impact of land use change on agroecosystem hydrology and water balance (Irmak & Kukal, 2022). Evapotranspiration is an essential, yet often uncertain, variable in the study of ecohydrological systems, which can account for as much as 95% of the water balance in dry areas (Wilcox et al., 2003). Hence, enhancing our understanding of *ET* and its components is crucial, as they offer valuable insights into water and heat transfer across the entire soil-plant-atmosphere continuum (Katul et al., 2012; Wang et al., 2015). As these two components have distinctly different roles within ecosystems (Kool et al., 2014), there has been increasing emphasis on the need to differentiate and measure the two components of *ET* separately (Wang et al., 2015). Partitioning *ET* components not only improves our understanding of the water budget but also enhances our knowledge of plant water use efficiency and biogeochemical cycles (Austin et al., 2004; Newman et al., 2006). From a crop production standpoint, transpiration is regarded as a beneficial water loss, as it is closely tied to essential biological processes promoting plant growth and biomass accumulation. In contrast, soil evaporation is considered non-productive water loss since it does not contribute to biomass production (Xiao et al., 2016; Yu et al., 2022). Therefore, reducing *E* is particularly important in the context of rainfed agriculture, which is more susceptible to the impacts of droughts than irrigated systems, requiring practices that minimize system-scale water use while maximizing productive water use by crops.

1.2 Evaporation Measurement

Evaporation from soil is a crucial component in the water balance of both natural and cultivated systems, accounting for about 20-40% of the global ET (Merlin et al., 2016). As water-limited environments currently make up nearly half of the Earth's land surface and are projected to expand further (Newman et al., 2006), the need for precise assessment of these evaporative losses has become increasingly critical (Kool et al., 2014). The techniques for measuring soil water evaporation include energy balance (micrometeorology) and water balance approaches (Xiao et al., 2011). The Bowen ratio (Fritschen & Fritschen, 2005; Zeggaf et al., 2008) and eddy covariance (Meyers & Baldocchi, 2005) approaches are commonly used micrometeorological methods for estimating soil evaporation over a large area. The automatic weighing lysimeter (Rumana, 2015), manual weighing lysimeter (Boast & Robertson, 1982; Da Rocha et al., 2022) and the soil water depletion method (Böhm et al., 1977) are other well-known approaches used in estimating soil evaporation by tracking changes in soil water storage and other water balance components. These techniques have been commonly employed in field studies to investigate water balance dynamics at or near the soil surface. However, micrometeorological techniques are not suitable for measuring evaporation from small experimental plots and rely on algorithms to estimate evaporation from vegetated surfaces. On the other hand, small lysimeters can be used to measure soil evaporation from small areas but are labor intensive, affect soil water processes inside the lysimeters and are only suitable to measure soil evaporation for short time periods (Han et al., 2017; Xiao et al., 2011).

1.3 Sensible Heat Balance Method

A measurement approach has been developed for continuous soil water evaporation (Heitman et al., 2008a, 2008b) determination based on sensible heat balance (SHB) theory of Gardner & Hanks, (1966). This approach uses a multi-needle HP probe to determine soil temperature and thermal properties, which are then used to solve the near-surface heat budget providing continuous millimeter-scale heat transfer and evaporation (Trautz et al., 2014; Xiao et al., 2016). The advantages of this technique include the ability to continuously measure sub-surface evaporation (Wang et al., 2021), and to capture millimeter-scale evaporation profiles over both a drying event (Deol et al., 2012) and during consecutive wetting-drying cycles (Xiao et al., 2011).

So far, a limited number of studies have utilized the combined HP and SHB method, whether by numerically simulating soil thermal and hydraulic processes or conducting field and laboratory experiments (Trautz et al., 2014). The SHB approach of determining soil evaporation was first implemented by (Heitman et al., 2008a) to compute Stage 2 evaporation rates in a bare surface field plot in central Iowa using three-needle heat pulse probes. Heitman et al. (2008b) compared daily subsurface evaporation from SHB with microlysimeter and Bowen ratio evaporation estimates and reported strong agreement between the results. However, according to Heitman et al., (2008a), their three-needle HP probe design with 6 mm needle spacing was unable to record evaporation from the top 3-mm layer of soil as the topmost heat flux was estimated at 3mm. Since it was also unclear whether the HP method could be used to measure evaporation over consecutive days, particularly during wetting-drying sequences, Xiao et al. (2011) evaluated the

SHB method for tracking subsurface cumulative evaporation over time and at various depths in a bare field across multiple wetting-drying cycles. Their findings demonstrated good agreement between SHB estimates and those obtained using the Bowen ratio technique. The SHB method was also evaluated by Sakai et al. (2011) by using numerically generated water contents, temperatures, and thermal properties under both constant and variable atmospheric conditions. Their results showed that this approach was effective in modeling the two stages (Stages 1 and 2) of evaporation of soil water. They also discovered that using smaller temperature sensing spacing reduced the undetectable zone (the layer of soil located between the top needle and the midpoint between the top two needles of a probe) and improved accuracy of evaporation rates. Xiao et al., (2012) developed an 11-needle heat pulse sensor with closer needle spacing i.e. 1-2 mm, to enhance the resolution of evaporation in the "undetectable zone". Deol et al. (2012) employed the 11-needle design to estimate evaporation under controlled laboratory conditions at soil depths as shallow as 0.5 mm. Xiao et al., (2014) conducted a study to implement the approach in a full-canopy maize field in Ames, Iowa. They also used a modified SHB method, incorporating below-canopy net radiation to account for Stage 1 evaporation, and demonstrated good potential of the SHB and modified SHB methods for estimating soil evaporation in a cropped field. Furthermore, Trautz et al., (2014) conducted a laboratory experiment combining the HP and SHB methods to compare laboratory experimental data to both an analytical and a fully coupled heat and mass transfer model. Their results showed that evaporation rates estimated using both modeling approaches were in close agreement with the experimentally measured evaporation rates, thus confirming the applicability of combined HP and SHB method to determine evaporation rates.

The SHB approach is based on the main assumption that the heat flow is one-dimensional (Heitman et al., 2020) and convective heat transfer is negligible (i.e., there is no heat transfer due to liquid water flow in soils) (Kojima et al., 2016), which may not be true shortly after rainfall events. Nonetheless, soil thermal property measurements, and consequently SHB-based soil evaporation, can be greatly influenced by heterogeneity, temperature gradient and ambient temperature fluctuations near the soil surface in the field (Heitman et al., 2020). Even though the combined HP and SHB method provides high-temporal resolution and continuous determination of soil evaporation with minimum soil disturbance (Liu et al., 2020), precisely installing these three-needle heat pulse probes is challenging, and placement errors can result in measurement inaccuracies (Xiao et al., 2012).

1.4 Heat Conduction Model

Soil thermal properties impact how energy is partitioned at the ground surface and influence heat and water transport across the ground surface (Ochsner et al., 2001). By governing the storage and movement of heat in soil, soil thermal properties influence soil temperature and heat flux as a function of time and depth (Abu-Hamdeh, 2003). Therefore, accurate determination of soil thermal properties becomes essential for solving the near-surface heat balance to estimate soil evaporation. To date, most studies on SHB-based evaporation determination have utilized Infinite Line Source (ILS) theory (Bristow et al., 1994) and the simplified equation by Knight & Kluitenberg, (2004) for determining soil thermal diffusivity (κ) and volumetric heat capacity (C) respectively. The ILS model is the most used framework for simulating the temperature change ΔT (ºC) measured at the apparent distance r_a (m) from a line-source heater in porous media. It is a solution of the heat conduction equation, derived by assuming that heat is released from an infinitely long line source into a homogeneous and isotropic medium. Heat is released from the line source at rate q' (W m^{-1}) during the time interval $0 < t \leq t_0$, where t is the elapsed time (s) from the initiation of heating and t_0 is the heating duration (s) (i.e., a few seconds). The solution is written as (Bristow et al., 1994):

$$\Delta T(t) = \begin{cases} -\frac{q'}{4\pi\lambda} Ei\left(-\frac{r_a^2}{4\kappa t}\right) & 0 < t \leq t_0 \\ \frac{q'}{4\pi\lambda}\left\{Ei\left[-\frac{r_a^2}{4\kappa(t-t_0)}\right] - Ei\left(-\frac{r_a^2}{4\kappa t}\right)\right\} & t > t_0 \end{cases} \quad [1.1]$$

where $-Ei(-z)$ is the exponential integral function of argument z. The main source of error for the ILS model lies in the assumptions that a heat pulse is applied from a line-source heater with zero radius and that the thermal properties of the needles have a negligible effect on the heat transfer, failing to account for the needles' finite physical dimension (cylindrical geometry) and thermal properties that differ from those of the surrounding soil (Meng et al., 2023). Neglecting the finite physical and thermal properties of the needles can, however, result in significant bias in thermal property estimation (Hopmans et al., 2002). Recent HP probe designs with finite physical dimensions violate the conventional ILS theory assumption, leading to inaccuracies in thermal property estimation. Furthermore, accurate determination of soil thermal conductivity (λ), which is defined as the product of κ and C, appears to be the most important component in the calculation of the heat balance method (Sakai et al., 2011). The identical-cylindrical-perfect-conductors (ICPC) model of Knight et al., (2012) yields more accurate estimates of soil thermal properties compared to ILS model (Lu et al., 2013) by accounting for the finite radius and finite heat capacity of the needles. Moreover, most studies using the SHB method have been using space-averaged λ in computing heat flux component of the heat balance. However, the numerical simulations by Sakai et al., (2011) found that using locally determined λ between each heater needle and temperature sensor needle yielded more accurate estimates of subsurface evaporation rate from the heat balance method rather than averaging λ across both sides of a heater needle. Nevertheless, the question of how the use of ICPC model and locally defined λ affect SHB estimated evaporation has not been fully examined.

1.5 Outline and Objectives

We propose to validate the combined HP and SHB method with an appropriate heat transfer model for better estimation of soil thermal properties, soil heat flux and consequently subsurface soil water evaporation. There are only a few comparative studies (Heitman et al., 2008b; Xiao et al., 2011, 2014) that evaluated the capability of SHB method for measuring evaporation with depth and time. Therefore, our study aims to evaluate the potential of SHB estimated evaporation using the heat pulse technique. Chapter 2 of this thesis focuses on the determination of soil thermal properties and near-surface soil heat flux using three-needle heat pulse probes. In Chapter 3, subsurface soil evaporation is quantified using the combined HP and SHB, and the results are compared with evaporation estimates from the eddy covariance method. Additionally, the third chapter tests the SHB method by comparing daily evaporation estimates with those obtained from microlysimeters.

Chapter 2 - Near-Surface Soil Heat Flux and Storage Measurement using Heat Pulse Probes

2.1 Abstract

Energy balance studies require measurements of soil heat flux and heat storage but traditional heat flux plates often underestimate soil heat flux and cannot be used near soil surface. Heat pulse (HP) probes are ideally suited for heat flux measurements near the soil surface due to their small size and ability for direct measurement of soil thermal properties. This study aims to apply three-needle heat pulse (TNHP) probes to estimate soil thermal properties and to measure soil heat flux and change in heat storage near the soil surface. TNHP probes were used to monitor soil volumetric heat capacity (C), thermal conductivity (λ), and soil temperature gradient in the inter rows of corn plants at a commercial corn field in central Kansas during natural wetting/drying cycles. HP probes were installed at ten depths beginning just below the soil surface (0.6 cm) and extending to a maximum depth of 7.2 cm. Soil sensible heat flux densities at different depths of the profile indicated a decline in amplitude as well as time lag in heat flux peaks with increasing depth. Soil sensible heat storage showed lower values (i.e. -7 to 12 W m^{-2}) compared to heat flux at all depths, and gradually decreased with depth. The temporal and spatial variation in soil thermal properties, heat flux and heat storage captured by the heat pulse probes were consistent with the variation in environmental factors, like net radiation and rainfall. Potential applications of this technique include location of the depth and magnitude of subsurface evaporative fluxes following the theory of sensible heat balance.

2.2 Introduction

Surface soil heat flux (G_0), a critical component of the surface energy balance (Gao et al., 2017; Leuning et al., 2012), comprises a significant portion of the net radiation (R_n) with values ranging from 20 to 40% under partial canopy cover (Kustas et al., 2000), and exceeding 50% of R_n for bare soil (Heusinkveld et al., 2004). Heat flux measurements at the soil surface are important to understand the drivers of water, energy, and trace gases exchange between the land and the atmosphere. Hence, accurate estimation of soil heat flux becomes crucial for various applications, including mesoscale land surface modeling, field-scale energy balance assessments, and understanding local soil temperature fluctuations in both managed and natural environments (Heitman et al., 2010). However, direct measurements of heat flux at the soil surface are not feasible. Instead, soil heat flux is typically recorded at a specific reference depth (G_r), and the surface heat flux is then derived by adding this reference flux to the change in heat storage (ΔS) occurring above the reference depth (Ochsner et al., 2007).

The most used approach for measuring soil heat flux is the combination method (Fuchs & Tanner, 1968). This method relies on heat flux plates inserted into the soil horizontally at a reference depth to measure G, while the heat storage in the soil layer above the plates is calculated using calorimetry (Hanks & Jacobs, 1971). Although heat flux plates are useful, they have often been found to underestimate soil heat flux because of low plate thermal conductivities, thermal contact resistance, and latent heat transfer effects (Ochsner et al., 2006). This requires the use of self-calibrating heat flux plates or additional corrections to obtain accurate soil heat flux data. However, G_r from heat flux plates is rarely corrected for measurement errors due to the limited availability of field thermal conductivity (λ) data (Peng et al., 2017). Nevertheless, precise estimates or measurements of λ near the soil surface are necessary if G_0 is to be determined for use in energy balance or evaporation equations (Sauer & Horton, 2005). Additionally, heat flux plates are not suitable near the soil surface due to their relatively large size as they can result in soil disturbance during installation (Ochsner et al., 2006).

Heat pulse probes (HPP) are ideally suited for near-surface heat flux measurements. HPP is a thermal sensor that can be used to derive thermal properties for soil and other materials using the temperature response curve to a heat pulse (Campbell et al., 1991) Thermal properties are obtained by fitting a heat transfer model to the measured time-series of temperature response to the heat pulse. HPPs have been widely used for the determination of a variety of indirect properties and processes of porous materials (e.g., soils) due to their ability to directly and simultaneously measure ambient temperature and thermal properties. Moreover, their small size and sample volume make them particularly useful for studying water processes near the soil surface (Ham & Benson, 2004). Bristow et al., (1994) introduced the first technique capable of simultaneously measuring all three soil thermal properties: thermal diffusivity (κ), volumetric heat capacity (C) and λ using the dual probe heat pulse (DPHP) sensor developed by Campbell et al., (1991).

The DPHP sensor was initially developed for measuring soil specific heat (Campbell et al., 1991). It typically consists of two parallel hypodermic-tubing needles, separated by a short distance, extending from a small sensor body, where one needle contains a heater made of resistance wire and the other contains a temperature sensor (thermocouple or thermistor). A current pulse of finite duration is applied to the heater element, generating a heat wave dissipating in all directions around the heater needle. As the heat moves through the surrounding soil, the temperature increase is detected by the temperature sensor in the adjacent needle. This temperature response is then evaluated for determining soil thermal properties. Previous studies have utilized DPHP sensors for various applications, such as measuring soil water content under both laboratory and field conditions (Heitman et al., 2003; Kamai et al., 2015; Tarara & Ham, 1997), for determining plant water uptake (Song et al., 1999) and the amount of water released by hydraulic lift in sunflower (*Helianthus annuus* L.) (Song et al., 2000). DPHP sensors provide an economical solution for simultaneously measuring soil temperature, volumetric water content, and thermal properties (Valente et al., 2018).

A modified HPP three-needle design (Ren et al., 2000) has been used to measure soil thermal properties as well as near-surface soil heat flux and evaporation (Heitman et al., 2008a; Heitman et al., 2008b; Xiao et al., 2011). Heat-pulse technique enables direct calculation of soil heat flux using the gradient method (Cobos & Baker, 2003; Kool et al., 2016). Furthermore, unlike traditional heat flux plates, the small needles of these HPPs allow their installation with minimum soil disturbance, while promoting good soil-sensor contact.

Most of the previous studies using HPPs (Peng et al., 2017; Wang et al., 2017; Zhang et al., 2020; Zhang et al., 2014) used thermocouples as temperature sensors, which have limited accuracy, may require signal amplification, and can also be susceptible to electrical noise. On the other hand, thermistors as temperature sensors are recognized for their higher sensitivity to temperature changes as compared to thermocouples (Ham & Benson, 2004), which provides an advantage for thermal property determination along with the measurement of temperature gradients (Kojima et al., 2016). However, biases among thermistors can lead to significant overestimation or underestimation of the temperature gradient between adjacent thermistors (Kool et al., 2016). This underscores the importance of calibrating the thermistors of heat pulse probes, as soil temperature gradient plays a crucial role in heat flux calculations.

Even though the modeled temporal temperature response to heating yields all three thermal properties (C, κ, and λ), their accuracy largely depends on precisely determining the apparent probe spacing (r_a) between the heater needle and adjacent temperature-sensing needles (Peng et al., 2021; Wang et al., 2017; Zhang et al., 2020) as well as on the selection of the soil heat transfer model (Kamai et al., 2015). Campbell et al., (1991) indicated that a 2% uncertainty in r_a can lead to a 4% relative error in C with heat pulse probes. Ensuring that probe spacing is determined accurately is essential for thermal property determination.

So far, most of the HPP studies (Wang et al., 2021; Xiao et al., 2014; Zhang et al., 2014) have used the infinite line source (ILS) model for the estimation of soil thermal properties, which assumes the heater needle to behave as an infinite line source releasing heat instantaneously (Campbell et al., 1991) or over a finite time interval (Bristow et al., 1994) to the surrounding medium. However, recent HPP designs (Kamai et al., 2015; Peng et al., 2021) with thicker needles violate the ILS model's main assumption, i.e., the probe needles have infinite length and zero diameter. Knight et al., (2012) proposed a semi-analytical solution that accounts for the effect of a finite needle radius and the finite heat capacity of both heater- and temperature-sensing-needle including the stainless-steel tubing and the epoxy. This new semi-analytical HPP model is called the ICPC model and has been found to yield more accurate estimations of thermal properties than the ILS model for agar-stabilized water (Naruke et al., 2021), as well as for specific soil materials such as sand and loam (Peng et al., 2021) with known thermal properties. In this study, the ICPC model was used for determining soil thermal properties.

The objectives of this study were to 1) to assess the temperature variability among the needles of the same probe and develop corrections to minimize possible temperature biases; 2) to derive the probe spacing for each probe by fitting the ICPC model to data collected for agar-stabilized water; 3) estimate near-surface soil thermal properties, heat flux, and heat storage in a commercial corn field and 4) investigate how environmental variables affect the dynamics of thermal properties, heat flux and heat storage under field conditions.

2.3 Theory

2.3.1 Soil Sensible Heat Flux and Change in Heat Storage

Fourier's law of heat conduction states that the rate of conduction per unit area is given by the product of the thermal conductivity of a solid or motionless fluid, e.g. soil in this study, and the temperature gradient:

$$G = -\lambda \frac{dT}{dz} \quad [2.1]$$

where G is the soil heat flux by conduction (W m^{-2}), λ is the thermal conductivity of the soil (W m^{-1} $^{o}C^{-1}$), and dT/dz is the temperature gradient (^{o}C m^{-1}). The minus sign indicates that the heat moves to the direction of decreasing temperature.

For a steady flow of heat between two parallel surfaces separated by a uniform layer, G can be determined by integrating Eq. 2.1:

$$G = -\lambda_n \frac{T_i - T_{i-1}}{z_i - z_{i-1}} \quad [2.2]$$

where i is the depth index, and λ_n is the soil thermal conductivity for depth layer z_i and z_{i-1}.

The change in soil sensible heat storage ΔS (W m^{-2}) for a uniform layer can be computed following Massman, (1993):

$$\Delta S = \sum_{i=1}^{N} \overline{C_s} \frac{dT}{dt} (z_i - z_{i-1}) \quad [2.3]$$

where $\overline{Cs}$ is the depth-averaged volumetric heat capacity of soil, z (m) indicates depth, and the subscript i is the index variable for a depth layer.

2.3.2 ICPC Model

Knight et al., (2012) proposed a semi-analytical solution to the temperature rise over time at the temperature-sensing needle, referred to as the ICPC model, given by

$$\widehat{T_C}(p) = \frac{q' K_0(\mu r_c)}{2\pi\lambda p\left\{\mu a_0\left[K_1(\mu a_0)+\left(\frac{\mu a_0 \beta_0}{2}\right)K_0(\mu a_0)\right]\right\}^2} \qquad [2.4]$$

where p is the Laplace transform variable (s^{-1}) and $\hat{T}_C$ (p) is the Laplace transform of the temperature at the temperature-sensing needle, T_C (t), for the case of continuous heating. Also, $K_n(z)$ is the modified Bessel function of the second kind of order n and argument z, $\mu = \sqrt{p/\kappa}$, a_0 is the radius of the needle (m), $\beta_0 = C_0/C_v$ where C_0 (J m^{-3} $^oC^{-1}$) is the volumetric heat capacity of the needle and C_v (J m^{-3} $^oC^{-1}$) is the volumetric heat capacity of the soil. The weighted average volumetric heat capacity of the needle, C_0, including stainless-steel and epoxy was calculated as:

$$C_0 = C_E \frac{d_E^2}{d_0^2} + C_{SS}\left(1 - \frac{d_E^2}{d_0^2}\right) \qquad [2.5]$$

where C_E (J m^{-3} $^oC^{-1}$) and C_{SS} (J m^{-3} $^oC^{-1}$) are volumetric heat capacities of the thermal compound within the needle and stainless-steel, and d_E (m) and d_0 (m) are the inner and outer diameter of the stainless-steel needle, respectively. Based on the principle of superposition, the temperature increase from pulsed heating can be calculated as:

$$\Delta T(t) = \begin{cases} \Delta T_C(t) & 0 < t \leq t_0 \\ \Delta T_C(t) - \Delta T_C(t - t_0) & t > t_0 \end{cases} \qquad [2.6]$$

This solution accounts for the effect of a finite needle radius and the finite heat capacity of both heater- and temperature-sensing-needle including the stainless-steel tubing and the epoxy. Knight et al., (2012) show that in case of needles with the same radius and heat capacity, their finite properties have equal influence on the heat-pulse signal received by the temperature needle. The ICPC model becomes identical to the ILS model of (Bristow et al., 1994) if the radius of both heater- and temperature-sensing-needle become zero (a_0 = 0). The introduction of finite needle radius (a_0) and β_0 accounts for the shift of heat-pulse arrival at the temperature-sensing needles relative to the ILS model, reducing the bias of thermal property estimation in materials with a varied range of thermal properties.

Knight et al., (2012) used the algorithm of Stehfest (Stehfest, 1970a, 1970b) with 16 weighting coefficients to invert the ICPC Laplace solution numerically. Knight et al., (2012) provide a complete description of this inversion procedure in their appendix B. In this study, we converted their original MATLAB code to a Python script to invert the semi-analytical Laplace solution for the temperature of the temperature needle and used the same weighting coefficients listed in their paper (Table B1) to perform the inversion.

2.4 Materials and Methods

2.4.1 Three-Needle Heat Pulse Probe Construction

We constructed TNHP probes (Figure 2-1) adapting previous probe designs (Ham & Benson, 2004). Each probe consisted of three needles made from 18-gauge stainless steel hypodermic tubing with outer and inner diameters equal to 1.27-mm and 0.838-mm, respectively. The hypodermic tubing was custom cut to 3.6 cm length, deburred, and flanged on one end. Each needle contained a thermistor (10K3MCD1, ± 0.2ºC resolution, BetaTherm Corp., Shrewbury, MA), positioned at 2.3 cm from the base of the needle for measuring ambient soil temperature. The central needle provided the heat pulse and was constructed from two loops (four strands total) of a single enameled resistance wire (210 or 205 ohms m^{-1}, 40 AWG Nichrome 80, Pelican Wire Co., Naples, FL) resulting in an overall heater resistance of 840 or 820 ohms m^{-1}.

After positioning the thermistors and resistance wire, the hypodermic needles were filled with high-conductivity silver epoxy (Arctic Silver, Arctic Silver Inc., Visalia, CA) to hold heater and thermistors in place and to provide good thermal contact between the heater wire, thermistor and hypodermic tubing. The silver cure epoxy was preferred as its thermal conductivity is 2.5 times greater than commonly used Omegabond 101 epoxy (Omega Engineering, Stamford, CT) (Kamai et al., 2015), thus, increasing the thermal conductivity of the probes. The epoxy was injected into the hypodermic tubing using a disposable syringe connected to a ~1-cm long flexible plastic tube with a slightly smaller diameter than the hypodermic needles.

Once the epoxy had cured, the heater and thermistor wires protruding from the flared end of the needle were trimmed to a 10 mm length, stripped, and soldered to an 8-conductor 24 AWG shielded extension cable (9538060500, Belden Wire and Cable, Richmond, IN), joining six conductors to the thermistors, and two conductors to the heater. The wires were soldered using 0.5 mm thick Tin-Copper-Silver Rosin Core Solder (99Sn-0.7Cu-0.3Ag) (Mandala Crafts, Cedar Park, TX).

Heater and thermistor-needle assemblies were inserted into a custom-made 3D printed plastic body (K-State Technology Development Institute, KSU, Manhattan, KS) with the following dimensions: 2.4-cm length, 2-cm width, and 1-cm depth, manufactured from a mixture of proprietary plastic resins (Vero series, StrataCys, Eden Prairie). The 3D body was manufactured with a cavity (1.9 cm x 2 cm x 1 cm) and three orifices with 6 mm center-to-center spacing to house the three probe needles. After the needles and wire were placed inside the probe body, the body cavity was filled with a cast resin CR-600 (Micro Mark, Berkeley Heights, NJ) securing all connections between the probes and conductor cables. After the cast resin was cured, the resistance of the heater circuit and each thermistor was checked to ensure the integrity of the connections within the probe.

2.4.2 Probe Laboratory Measurements

2.4.2.1 Probes installation in water stabilized with agar

Water stabilized with agar provides a reliable standard medium with known volumetric heat capacity at room temperature as agar suppresses convective thermal gradients within its gel-like structure (Naruke et al., 2021). A 6g/L solution of agar-stabilized water was prepared by heating the mixture of water and agar (Bacto ™ Agar, Becton, Dickinson and Company, Sparks, MD, USA) to the water boiling point to ensure that the agar was completely dissolved in water. The probe wires were attached to a horizontal metal rod and their bodies were carefully lowered into 600 mL glass beakers. The agar solution was then poured into the beakers. Ten TNHP were centrally positioned facing downward, ensuring their needles and probe bodies were completely immersed in the agar-stabilized water. The beakers were then sealed using a thin plastic film to minimize moisture loss.

2.4.2.2 Data acquisition

The probes were connected to a data acquisition system, which consisted of a datalogger (Model CR3000, Campbell Scientific, Inc., Logan, UT) and two multiplexers (Model AM 16/32 and AM 16/32B, Campbell Scientific, Inc., Logan, UT) for reading the signal from thermistors sequentially. The resistance from the thermistors was measured using a four-wire half-bridge measurement circuit with a 5000-Ω reference resistor (0.1% tolerance, S102K series, Precision Resistor Company, Largo, FL) for each multiplexer.

During the temperature measurement cycle, the datalogger scanned all probe thermistors every 10 seconds and recorded the average temperature for 30-min intervals. During the thermal property determination cycle, the three thermistors of a single probe were scanned at 1-s intervals to capture the increase of temperature due to the heat pulse. Prior to applying the heat pulse, the thermistor temperatures were measured for a period of 10 s to obtain the background temperature. A relay controller (Model SDM-CD16AC, Campbell Scientific, Inc., Logan, UT) was used to supply power to the heater needle for 8 s. A 1-Ω shunt resistor (0.1% tolerance, Model VPR5, Vishay Inc., Malvern, PA) was inserted between the heater probe G terminal and the datalogger ground terminal. The voltage drop across the shunt resistor was measured at a frequency of 10 Hz. The thermal property measurement cycle was performed every four hours in which each probe temperature was monitored for 120 seconds. One-second temperature data and average shunt-resistor voltage were recorded for each probe during the thermal property measurement cycle.

2.4.2.3 Apparent probe spacing estimation

The apparent probe spacing was estimated by fitting the ICPC model to the temperature data collected in agar-stabilized water (Section 2.4.2.1). Probe spacing between adjacent needles was determined by assuming that C of the agar solution is equal to that of free water i.e. 4.18 MJ m^{-3} $^{o}C^{-1}$ (Campbell et al., 1991; Ochsner et al., 2003). The ICPC model is appropriate for use in applications where the ratio of probe radius (a_0) and probe spacing (L) satisfies the condition that $a_0/L \leq 0.11$, which is true in our case ($a_0/L = 0.06$). r_a and κ were estimated by fitting the model to the measured $\Delta T(t)$ data using a nonlinear curve fitting algorithm (Newville et al., 2014). The liberty Lmfit (version 0.8.0) built on Levenberg-Marquardt algorithm of scipy.optimize.leastsq() from SciPy library in Python, was used for the non-linear least-squares optimization and curve fitting. The fitting was done iteratively using least-squares optimization techniques to minimize the residual between the model and the data.

2.4.2.4 Thermistor offset determination

The 30-min temperature averaged data obtained during the temperature measurement cycle (Section 2.4.2.2) was used to determine the needle temperature variability for a single probe. The average absolute difference between the temperature readings of the outer thermistors in reference to the central needle was calculated as the mean absolute error (MAE). Temperature offsets for the outer thermistors of the probe were calculated as the average deviation from the central thermistor temperature computed over a short time (~ 3 days):

$$T_{offset} = \frac{\sum_{t=1}^{N}(T_{c,t} - T_{a,t})}{N} \qquad [2.7]$$

where, T_c is the temperature at the central needle, T_a is the temperature at the outer needle, t is the time variable and N is the total number of observations.

The calculated offsets were then added to the original temperature measurements to compute the adjusted measurements. The difference between the adjusted thermistor measurements and the central thermistor measurements was again averaged to determine the MAE after the application of temperature offsets. The average MAE before and after applying temperature offsets were compared to assess the change in temperature differences between thermistors.

2.4.3 Field Experiment

2.4.3.1 Field site description

The field experiment was conducted at a commercial corn field in Gypsum, KS from May to July 2023. Corn was planted on May 1 with a row-spacing of 76 cm. The soil of the experimental site is mapped as Hord silt loam. Particle size analysis, determined using the hydrometer method (Gavlak et al., 2005), indicated the proportions of sand, silt and clay were: 18%, 58% and 24%, respectively. The average soil bulk density (ρb) was determined to be 1.33 (g cm^{-3}), which was estimated from six soil cores collected at 0 - 7.5 cm depth using ring samplers (7.62-cm diameter and 7.5-cm long).

Net radiation (R_n) was measured with a four-component net radiometer (NR01, HukselfluxUSA, Inc., Center Moriches, NY) at 1-m above the ground. Precipitation (P) was measured using a tipping bucket rain gauge (Model No. TRP525I, Texas Electronics Inc., Dallas, TX). The sensors were scanned at 10-s intervals using a datalogger (CR3000, Campbell Sci.) and average R_n and total P were computed for 30-min intervals.

2.4.3.2 Heat pulse probe measurements

Heat pulse probes were installed in between the rows of corn nine days after sowing. The soil surface was first cleared of all the debris and crop residue, and a shallow trench was excavated for probe installation. The portion of the vertical trench face into which the probes were installed (Figure A-1) was centered between two corn rows and perpendicular to row direction. A template for marking probe positions was fabricated by drilling 10 holes in a sheet of acrylic plastic. The template was placed against the trench face and finishing nails were pushed through the holes to mark the probe positions. At each position, a cavity large enough to accommodate a probe body was dug into the trench face. The probes were inserted by pushing their three needles into undisturbed soil behind the excavated cavities. Once installed, the bodies of probes fit snuggly within the excavated cavities. The HPPs were installed at ten depths beginning immediately below the soil surface with the central needles of the probes positioned at 12, 18, 24, 30, 36, 42, 48, 54, 60, and 66 mm (Figure 2-2). After installation, the probe conductor cables were routed away from the trench face, and the trench was carefully backfilled. The crop residue removed prior to probe installation was carefully placed back on soil surface.

The probe data acquisition was performed by the same system described in Section 2.4.2.2. For the field installation, the datalogger, multiplexers and control relay were housed in waterproof enclosures. Power to the system was supplied by a 12 V deep-cycle battery charged using a solar panel. Heat pulse measurements were collected every 6 hours for the duration of the study. The heat pulse measurement sequence for each probe consisted of background temperature measurement for 10 s, followed by 8-s heating of the central needle, and measurement of the temperature response at the outer probe needles for an additional 35 s. Heat pulse measurements were performed in a sequential order, beginning with the shallowest probe, followed by the probe directly beneath it, and then proceeding to the probe beside the shallowest one. This process was repeated until reaching the deepest probe in the soil profile.

After the thermal property measurement cycle finished, the probe thermistor signals were monitored at a 10 s interval and half-hour averages were recorded for soil temperature analysis.

2.4.3.3 Thermal property determination

The ICPC model was employed to estimate C and κ from the heat input and temperature response. In this model, with known heat input and r_a values, C and κ were determined by fitting the solution to the captured temperature rise data, and λ was calculated as the product of C and κ. The temperature response was corrected for the background temperature variation using the temperature measurements collected prior to the heat pulse initiation (Ochsner et al., 2006). To obtain soil thermal properties, the heat response data was fitted to the model using a non-linear curve fitting routine (Newville et al., 2014). The liberty Lmfit, a high-level package in the Python programming language, was used for the non-linear least-squares optimization and curve fitting. The standard errors, square roots of the diagonal components of the covariance matrix, were used to explain the uncertainty in the estimated parameters. Percentage standard error was calculated as the ratio of the estimated standard errors to their respective values of thermal property. Since thermal properties were obtained at 6-h intervals, linear interpolation was used to estimate half-hourly values of thermal properties used for heat flux and soil storage estimation.

2.4.3.4 Temperature gradient, heat flux, and heat storage measurement

Half-hourly measurements of soil temperature, heat flux and heat storage were obtained from probe data collected at depths ranging from 6 to 72 mm. Values of temperature gradient ($\Delta T/\Delta z$) (Section 2.3.1) were computed from the temperature difference between adjacent needles of the same probe divided by the spacing between the needles. The temperature gradient was assigned to the midpoint depth between the needles, and thermal conductivity determined for the same depth layer between the two needles was then multiplied with the respective $\Delta T/\Delta z$ to compute heat fluxes G_1 and G_2 (W m^{-2}) for each probe.

For determining the soil temperature time derivative (dT/dt) required for the soil sensible heat storage ΔS (W m^{-2}) calculation, a third-order polynomial was fitted to the temperature data over a 4-hr window, and the time derivative of temperature for middle of the measurement period was computed using the coefficients of the polynomial function. For this calculation, C was averaged for each probe depth increment. ΔS was assumed to represent the depth increment between G_1 and G_2. Figure 2-3 shows the heat-pulse probe and measurement interpretation for sensible heat balance calculation.

2.5 Results and Discussion

2.5.1 Probe Laboratory Measurements

2.5.1.1 Apparent probe spacing estimation

Figure 2-4 shows the temperature response to the heat pulse recorded by an HPP. The curve fitting revealed strong agreement between the model and temperature data, with very low residual values ranging between -0.0024 ºC and 0.0046 ºC. Figure 2-5 shows the distribution of apparent probe spacing values between the central needle and each of the two outer needles for the ten probes calibrated in the laboratory. As the probe spacing values showed asymmetric distribution, with some noticeable outliers, r_a between the central and the adjacent needles was computed as the median of the readings. The average probe spacing and standard deviation for the ten probes were 6.04 mm and 0.05 mm, respectively. The probe spacing values obtained from the fitting were very close to the physical probe spacing i.e. 6 mm. This confirms the accuracy of the obtained r_a values provided by HPP data and the ICPC model. Nevertheless, pre-field deployment calibrations of probe spacing may not always accurately represent the spacing of buried probes. Using r_a can introduce large uncertainties in *C* values when probe deflections occur, particularly in dry soils with higher bulk density. Therefore, using robust probes with relatively short and thick needles to minimize the risk of probe deflection, and installing the probes when the soil is moist could be a valuable solution for long-term field experiments monitoring soil thermal properties using the HP method.

2.5.1.2 Thermistor offset determination

Figure 2-6 shows the temperature offset values for all outer thermistors of the ten HP probes calibrated in agar stabilized water. The offset values ranged from -0.1271°C to 0.0806°C. The MAE calculated relative to the central needle before applying offsets to the temperature readings ranged from 0.0057°C to 0.1264°C with an average of 0.0358°C. After applying the temperature offsets to the outer thermistors, the MAE relative to the central needle ranged from 0.001607°C to 0.0518°C with an average of 0.0033°C. The average MAE of 0.0033°C was less than an order of magnitude of the maximum offset of 0.0806°C.

Temperature offsets when applied to individual thermistors minimized the temperature difference between the three thermistors. Figure 2-7 shows half-hour average temperature readings recorded by the thermistors before and after the application of the temperature offsets for a selected probe. Overlapping of temperature curves after the application of temperature offsets and the decrease in MAE suggested that a single value of thermistor offset was able to account for temperature discrepancies between the individual thermistors. Kool et al., (2016) conducted a laboratory thermistor calibration using a similar thermistor with ± 0.01ºC resolution and found that the temperature offsets before and after field deployment, with 5 years in between, remained fairly constant with time. This suggests that pre- or post-experiment temperature calibration could ensure accurate temperature measurements.

2.5.2 Environmental Conditions

Net radiation varied around rainfall events, with maximum daily values typically exceeding 900 W m^{-2} (Fig. 2-8a). During the measurement period, the mean daily maximum and minimum air temperatures, measured at 2 m above ground, were 31.1° and 15.2 °C, respectively (data not shown). Rainfall was observed on 19 days throughout the period, with the highest daily totals for precipitation of 19 mm occurring on June 21 and July 4 (Figure 2-8b). Soil temperature recorded by the shallowest probe needle at 6 mm ranged between 12.7 °C and 34.2° C, while soil temperature at 66 mm recorded by the deepest probe in the profile ranged between 14.5 °C and 29.5 °C (Fig. 2-8c). Figure 2-8c shows a time lag in temperature peak occurrence recorded at 6 and 66 mm, as well as larger difference in daily maximum temperature towards the end of the measurement period.

2.5.3 Soil Thermal Properties

Figure 2-9 illustrates the time series of λ and C at three depths (9 mm, 27 mm, and 63 mm) within the soil profile. The percentage standard error for estimated C and λ values ranged from 0.028% to 0.925%. Both λ and C increase following rainfall. Although both properties are affected by moisture changes, C has a more direct linear relationship with the volume fraction of water (de

Vries, 1963), leading to a more rapid change during water internal drainage. Therefore, rainfall events caused sudden increases in *C*. In contrast, λ is a non-linear function of water content, hence the increase in λ is not as sharp as *C*. Additionally, the increase in *C* after rainfall is more pronounced in shallower depths i.e., at 9 mm, but after 2–3 days, the effect diminishes as soil properties limit further water movement. Drying in the upper portion of the soil profile also leads to a decrease of both *C* and λ. However, *C* declines more sharply right after rainfall events (Fig. 2-9b), whereas the decrease in λ occurs more gradually (Fig. 2-9c).

Both *C* and λ also increase with depth (Fig. 2-9b and 2-9c). The observed higher values of *C* at greater depths is likely due to higher moisture content in deeper layers as compared to the near-surface zone which tends to lose more moisture due to solar radiation exposure. Similarly, the increase in λ with depth may be explained by an increase in soil bulk density at deeper levels. Although bulk density measurements are not available for each layer to directly support this inference, it is assumed that deeper soils are more compacted. Given that denser soils generally contain a higher proportion of mineral constituents which possess greater λ than air or water, this would contribute to elevated λ values. The observed trend of higher λ at greater depths (Fig 2-9c) aligns with the findings of Lu et al. (2016), who demonstrated a linear relationship between λ and bulk density (ρ_b) in silt loam soils.

Furthermore, both thermal properties exhibit diurnal fluctuations (Fig. 2-9). The thermal properties of soil near the surface are influenced by cycles of wetting and drying. While the six-hour measurement intervals prevent detailed analysis of these patterns, the data suggest that thermal properties decrease from early evening to early morning and increase from midmorning to late afternoon, aligning with diurnal variations in near-surface soil moisture reported in a previous study (Heitman et al., 2003). Both *C* and λ are a function of soil water content, however, λ is more sensitive in the drier region (0–0.2 volumetric moisture content) (Jacobs et al., 2011). Capturing these daily fluctuations in soil thermal properties, especially λ in the near-surface zone, due to changes in soil moisture, can help in estimating the diurnal variation in subsurface soil heat flux.

2.5.4 Soil Heat Flux and Change in Heat Storage

2.5.4.1 Dynamics of net radiation, soil temperature gradient, soil sensible heat flux and heat storage

Figure 2-10 shows the time series of R_n measured by the net radiometer, soil temperature gradient, and soil sensible heat fluxes and heat storage at 9 and 15-mm soil depths (recorded by the shallowest probe in the profile) over 12 consecutive days (May 20 – 31) of the field study period. This corresponds to the period shortly after corn emergence, i.e., when the soil had no vegetation cover. R_n values ranged approximately between −70 to 1015 W m^{-2}, with daily maximums occurring between 10:00 and 14:30 and daily minimums between 20:00 and 01:00. A rainfall event of 5.4 mm was recorded in the evening of May 25.

The temperature gradient and sensible heat flux at the 9-mm depth were larger than those observed at 15-mm. Values of heat flux at 9 mm depth (G_9) ranged from -53 to 107 W m^{-2}, with daily maximum values corresponding to the daily maximum soil temperature gradients at 9-mm depth, occurring between 10:30 and 13:30. Heat flux at 15 mm depth (G_{15}) was observed between -34 and 67 W m^{-2}. For this depth as well, the daily maximum heat fluxes corresponded with the daily maximum temperature gradient. This suggests that soil temperature gradient played a key role in driving the heat flux. Over the 12-day period, the diurnal cycles of R_n and G_9 followed a similar trend and were roughly in phase with each other; daily maxima occurred between 10:00 and 14:30. On most days, the daily maximum G_9 exceeded 85 W m^{-2}, which corresponded to relatively large R_n values (above 900 W m^{-2}). Heat fluxes at these two depths only converged on days with lower R_n, such as May 22 and 25 (Fig. 2-10c).

The change in soil sensible heat storage (ΔS) between the two depths 9- and 15-mm ranged between -4.8 to 7.6 W m^{-2}. The amount of heat partitioned to ΔS remained consistently small throughout the period. Similar finding has been observed in a previous study investigating the depth and magnitude of subsurface evaporation in bare soil, where the magnitude of ΔS (3-9 mm) remained significantly lower than heat fluxes at 3 and 9 mm (Heitman et al., 2008b). The lower magnitude of ΔS compared to G_9 and G_{15} is likely due to only a small portion of heat energy being stored in the soil layer, while the majority was transferred. The heat storage always peaked earlier than the heat fluxes. This pattern was also consistent with the results of other studies (Lu et al., 2016, 2018) that determined sub-surface heat flux using gradient method. Furthermore, the gradual diurnal fluctuation in ΔS (Fig. 2-10c) could be because it is integrated over depth and time steps.

2.5.4.2 Variability of soil sensible heat flux and heat storage at different depths

Subsurface soil heat flux measurements at midpoint depths between the top and the central needle of all the HP probes in the soil profile are shown in Fig. 2-11. The study period spanned from shortly after corn emergence until after the closure of the canopy cover. Soil heat flux exhibited a characteristic diurnal pattern at all measured depths, with the largest amplitude observed at the 9-mm depth, followed by progressively lower amplitudes at greater depths. This attenuation of amplitude with depth could be attributed to the insulating properties of soil, which dissipated heat as it propagated downward. At 9 mm, heat flux values ranged from approximately -50 to 180 W m^{-2}, with daily maximum values occurring between 11:00 and 14:00 h and daily minimums between 23:00 and 04:00 h. The maximum recorded heat flux at this depth exceeded 100 W m^{-2} on most days, with the highest value of 179 W m^{-2} observed on June 24, coinciding with one of the days with relatively high net radiation of 1030 W m^{-2}. At 57 mm, heat flux values ranged from -40 to 95 W m^{-2}, whereas heat fluxes were approximately between -41 and 94 W m^{-2} at 63 mm depth.

A field experiment conducted in semi-arid grassland in China to compare ground heat flux measurements from heat pulse and plate methods revealed that the magnitude of sub-surface heat flux measured at various depths using a multi-needle probe declined with depth (Lu et al., 2018). The decline in heat flux magnitude was possibly because deeper soil layers experienced greater insulation from rapid surface temperature variations, leading to more stable thermal conditions and reduced daily fluctuations. The divergence in heat fluxes at various depths indicated a large heat sink within the soil profile associated with heat consumption for water vaporization (Heitman et al., 2008a). Time lag in the occurrence of the maximum heat flux at deeper depths suggests delay in the occurrence of maximum temperature at deeper layers of the soil profile.

The difference in peak daily heat flux between the 9-mm and 15-mm depths remained significantly larger throughout the study period, with fluxes at 9 mm reaching up to 50% higher than those at 15 mm. The maximum recorded difference in heat flux at these depths was 76.6 W m^{-2}. However, this difference gradually decreased with increasing depth, becoming minimal between the 57-mm and 63-mm depths. The maximum difference in daily peaks between the 27-mm and 33-mm layers was 46.6 W m^{-2}, whereas the greatest difference between the 57-mm and 63-mm depths was only 5.6 W m^{-2}, representing only 7.3% of the difference observed in the uppermost layer (9 - 15 mm). At these deeper layers, maximum daily heat fluxes generally ranged between 40 and 60 W m^{-2} for both depths. Soil heat flux appeared to increase progressively throughout the experiment, likely due to the greater availability of solar energy during the summer months.

Figure 2-12 illustrates the change in soil sensible heat storage (ΔS) for soil layers corresponding to the depth interval between the two points where heat fluxes were determined using a single probe. The relatively low ΔS values compared to the heat fluxes in the same soil layer suggest that most of the heat energy moved vertically through the soil profile, with only a small portion being stored in that layer. The magnitude of ΔS also declined with depth, due to greater insulation from soil layer above. ΔS ranged between 11.9 and - 6.9 W m^{-2} at the 9 – 15 mm layer. The maximum and minimum values for ΔS at 27 – 33 mm layer were 10.6 and -5.9 W m^{-2} indicating that they differed slightly from the 9 – 15 mm layer. However, ΔS at the 57 – 63 mm had a larger difference compared to 9 – 15 mm layer with values ranging from 6.8 to -3.5 W m^{-2}. Soil near the surface undergoes greater temperature variations because of direct exposure to solar radiation, air temperature shifts, and other environmental influences. However, these fluctuations decrease with depth, leading to a smaller change in sensible heat storage. The diurnal variation in ΔS was smaller compared to heat flux, as the storage or release of heat energy tends to change gradually, unlike the more abrupt shifts seen in heat flux. Overall, the amplitude and phase relationships with respect to depth were consistent with the expected behavior.

2.6 Conclusions

This study demonstrated that three-needle heat pulse probe is a viable method that provides accurate in-situ and continuous measurements of soil thermal properties in addition to sensible heat flux densities and change in heat storage. The small size and needle design of the heat-pulse probe make it possible to provide a spatial resolution of a few millimeters, which is ideal for measuring the highly dynamic near-surface soil thermal properties and heat flux. Laboratory correction for thermistors' temperature differences revealed that a constant offset can account for errors in measured temperature gradients. Pre-deployment calibration for apparent probe spacing revealed reasonable estimates of probe spacing values, which improves the accuracy of the soil thermal properties estimated using the ICPC model. Temporal and spatial analysis of soil sensible heat flux demonstrated that heat flux densities decreased in magnitude with depth, and temperature gradient was the major factor influencing the flux. Change in soil sensible heat storage showed lower values as compared to heat flux. The probe design limited our measurement of heat flux to the depth of 9 mm. Future experiments with improved design as used in previous studies could reduce this zone to as less as 0.5 mm. Furthermore, these estimations of soil sensible heat fluxes and change in heat storage, provide a way forward for determining the depth and magnitude of sub-surface soil water evaporation estimation following the theory of sensible heat balance in soil layers.

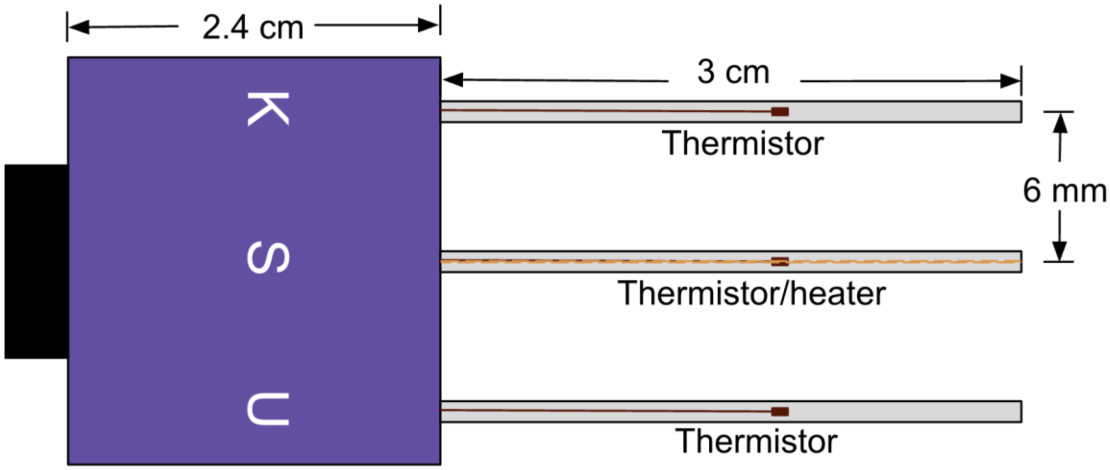

Figure 2-1 A schematic diagram showing a cross-section of a three-needle heat pulse probe. Each probe has three needles, with a thermistor (brown line), and the central needle has a heater (dashed orange line) made of resistance wire.

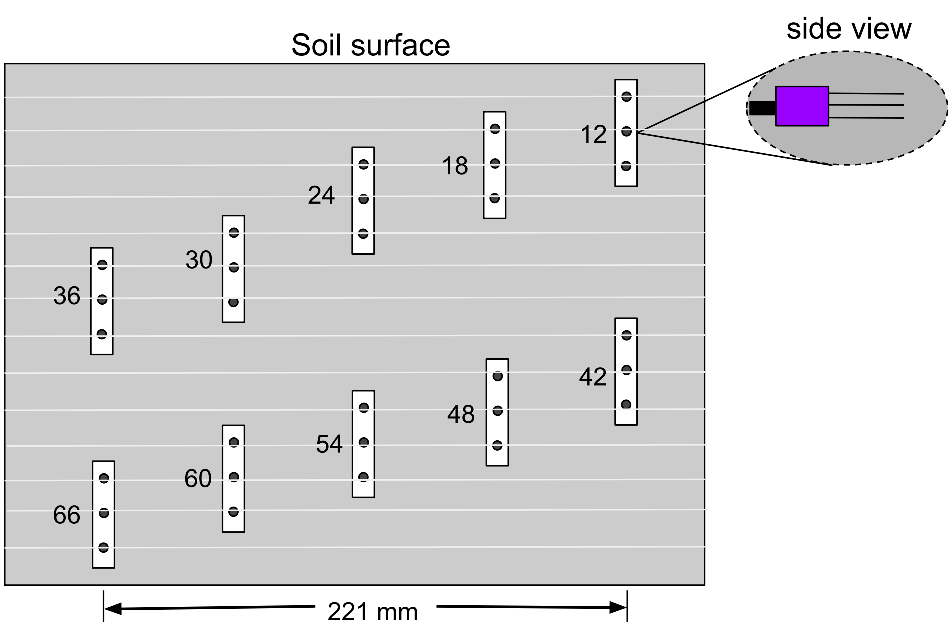

Figure 2-2 A cross-sectional view of the heat pulse probe installation in both sites. White rectangles are the probe bodies; dark-colored circles within the rectangles indicate the position of probe needles. Numbers beside each probe indicate the middle needle depth (mm). The diagram is not drawn to scale.

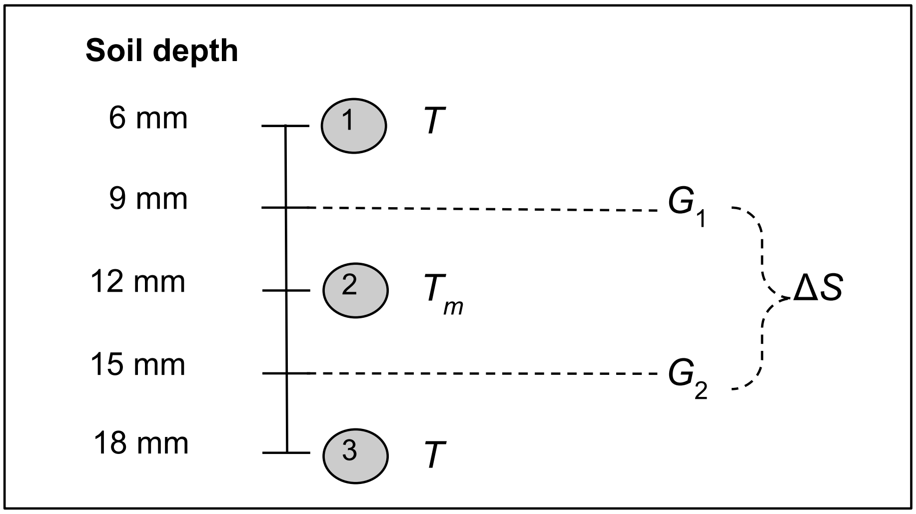

Figure 2-3 Heat-pulse probe and measurement interpretation for sensible heat balance calculation for the topmost probe in the profile. Symbols denote temperature (T), soil sensible heat flux (G_1 and G_2), and change in heat storage (ΔS).

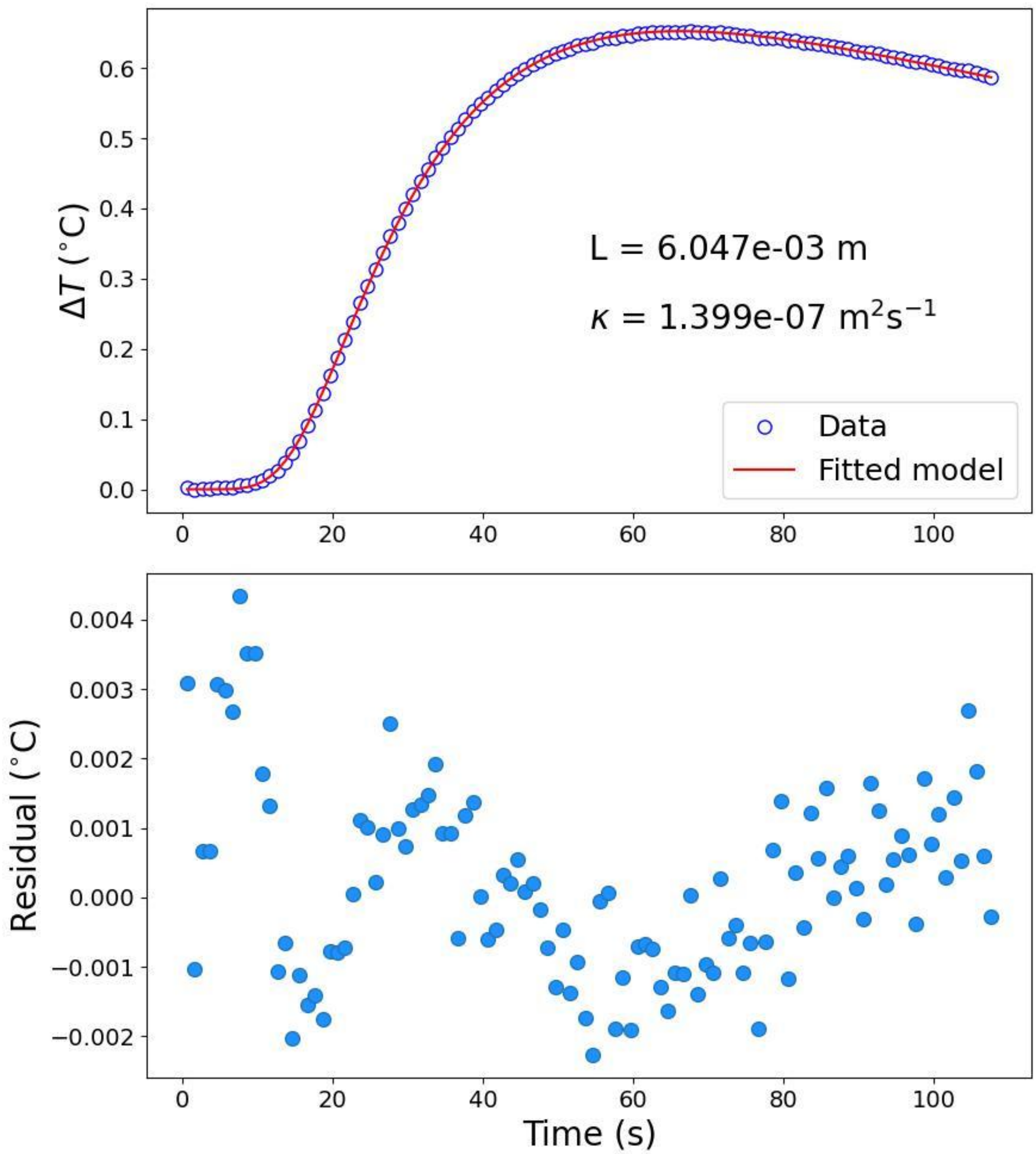

Figure 2-4 Curve fitting of heat pulse response data to the *ICPC* model to determine the apparent probe spacing between adjacent needles of a probe. *L* is the probe spacing value in m and κ is the thermal diffusivity of the agar solution.

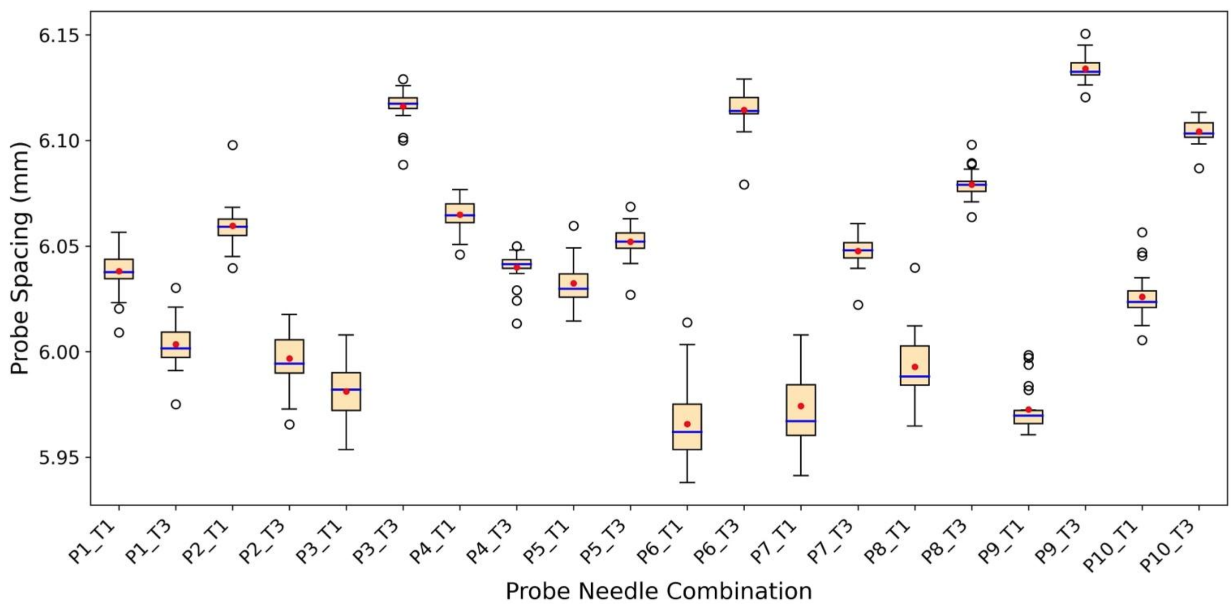

Figure 2-5 Apparent probe spacing values determined for each outer needle of the ten HP probes calibrated in the laboratory. The blue line in each box indicates the median, the red circle denotes the mean, and the bottom and top edges of the box mark the 25th and 75th percentiles, respectively. The whiskers are extended to the most extreme data point that is no more than 1.5 times the interquartile range (IQR) from the edge of the box. The circle represents outliers that lie beyond the whiskers.

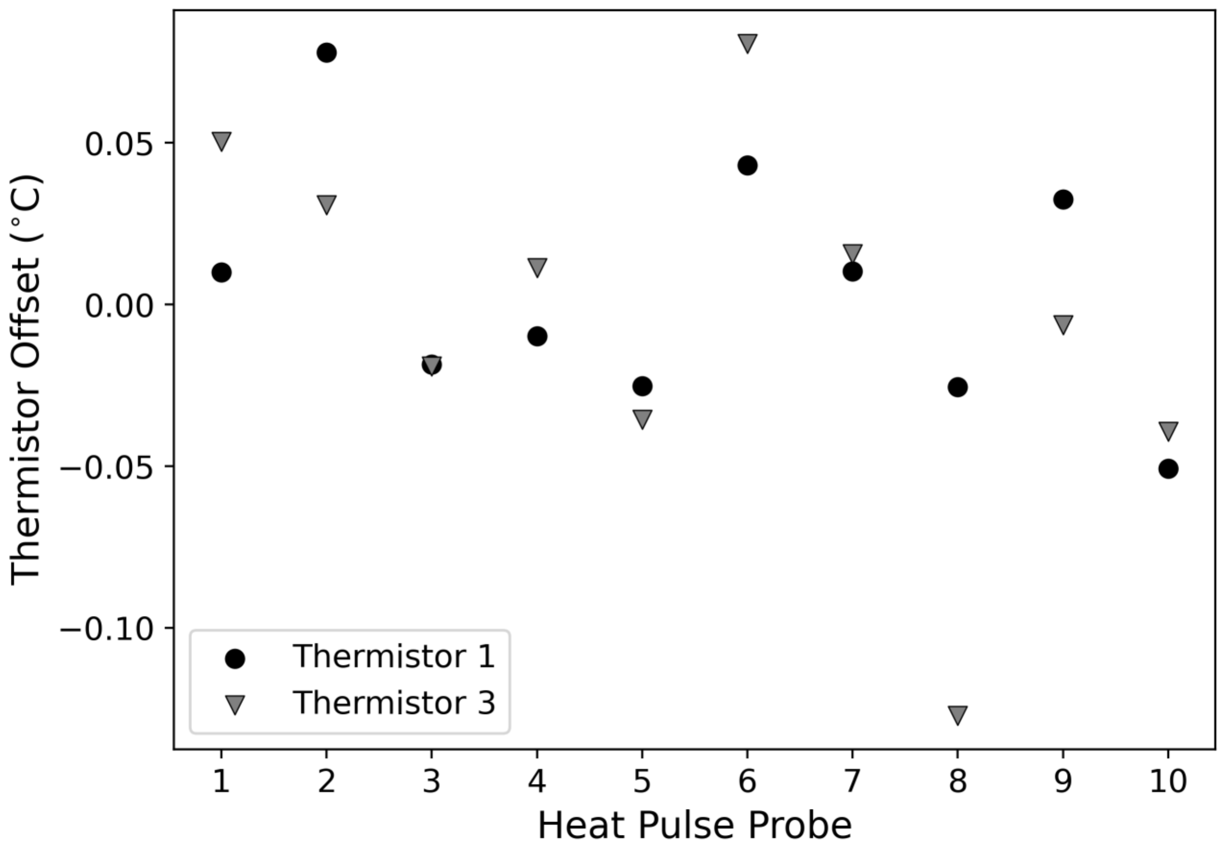

Figure 2-6 Thermistor offsets determined for each outer needle of the ten heat pulse probes (HPPs) calibrated in the laboratory.

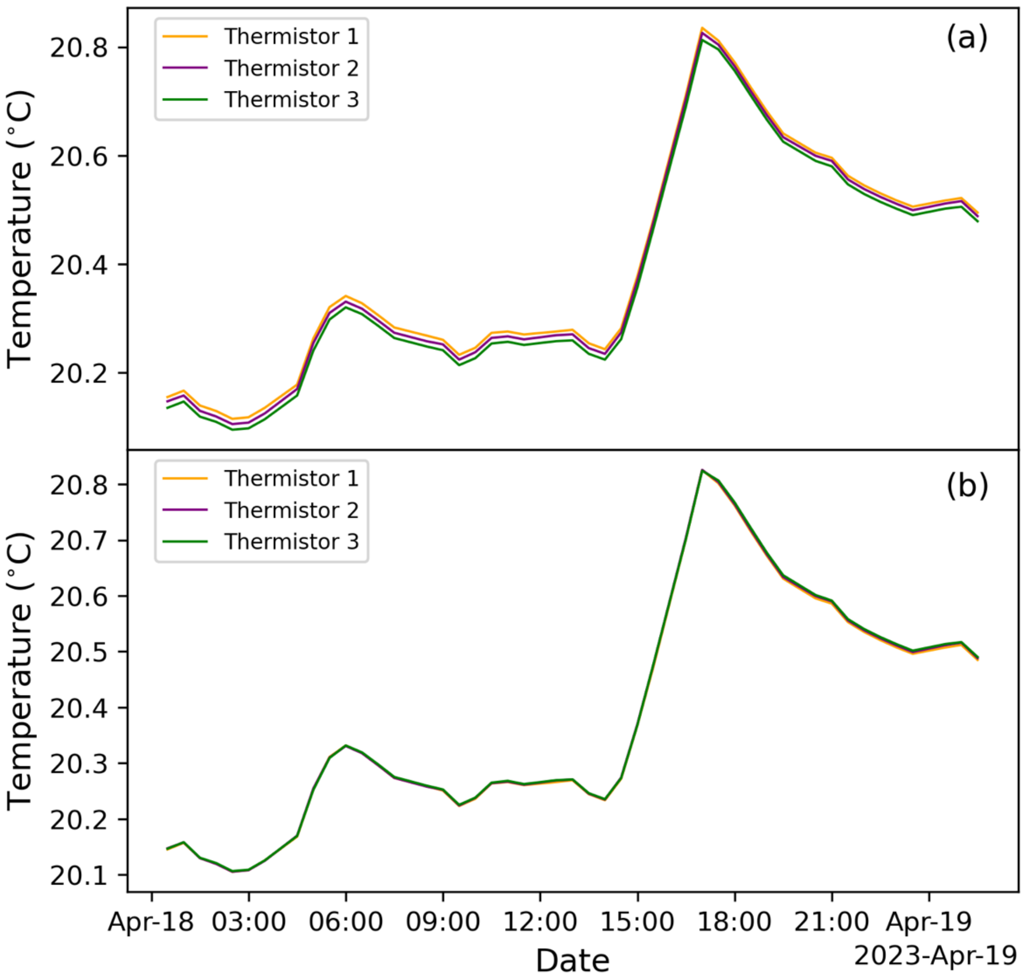

Figure 2-7 Agar temperature readings recorded by each thermistor of a heat pulse probe before (a) and after (b) application of thermistor offsets.

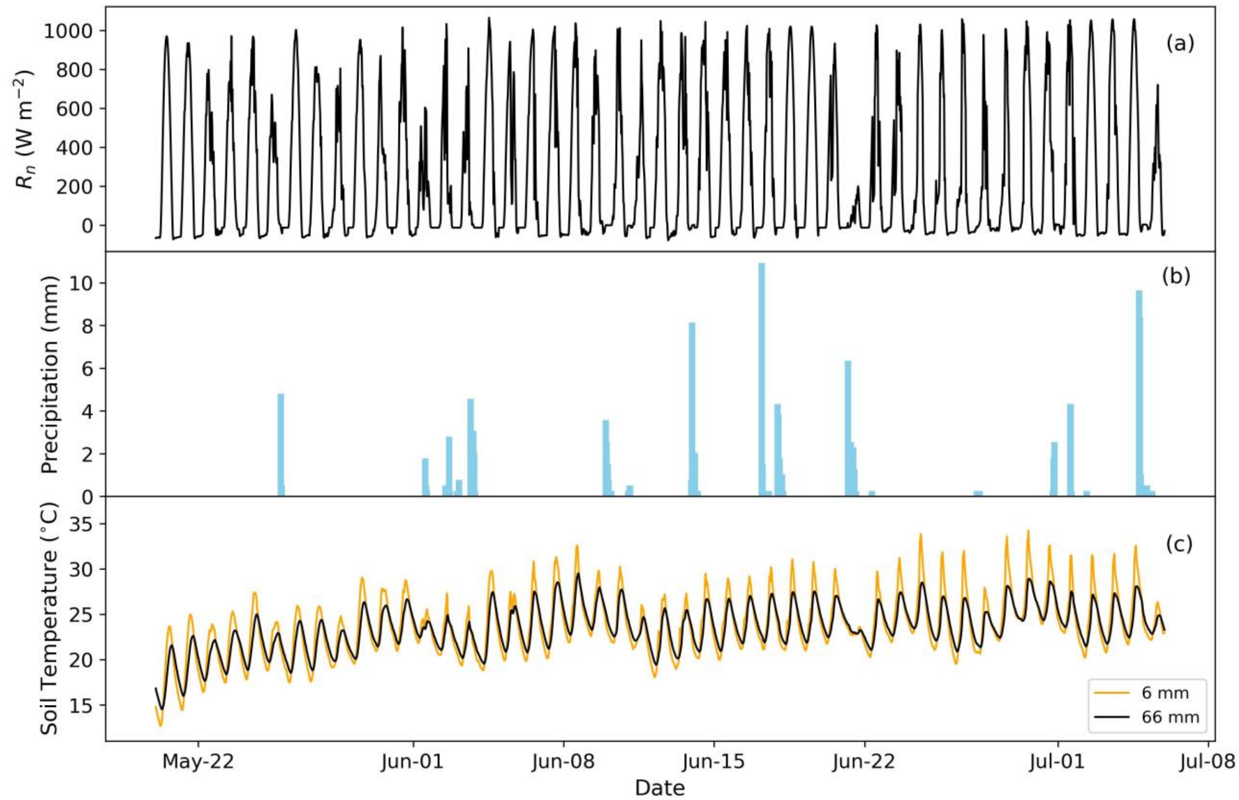

Figure 2-8 Half-hourly net radiation (Rn) values recorded by the net radiometer in the site (b) Hourly precipitation obtained from the Gypsum station of the Kansas Mesonet for the experimental period (c) Soil temperature recorded by the shallowest and the deepest heat pulse probe in the profile.

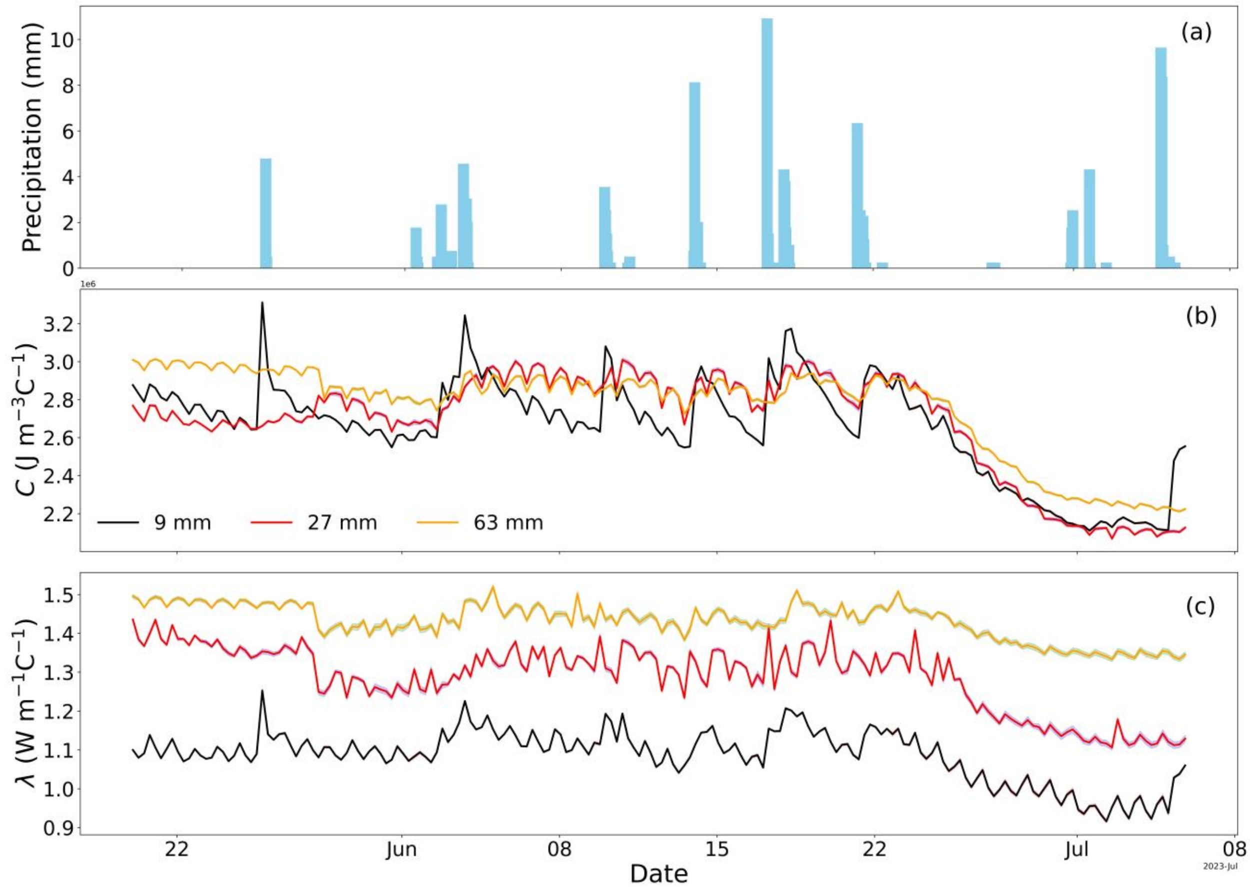

Figure 2-9 Hourly precipitation obtained from the Gypsum station of the Kansas Mesonet for the experimental period. (b) Soil volumetric heat capacity (*C*) and (c) thermal conductivity (λ) measured by heat pulse probes at three depths in the soil profile. Symbols in (b) and (c) indicate measurements recorded each 6 h.

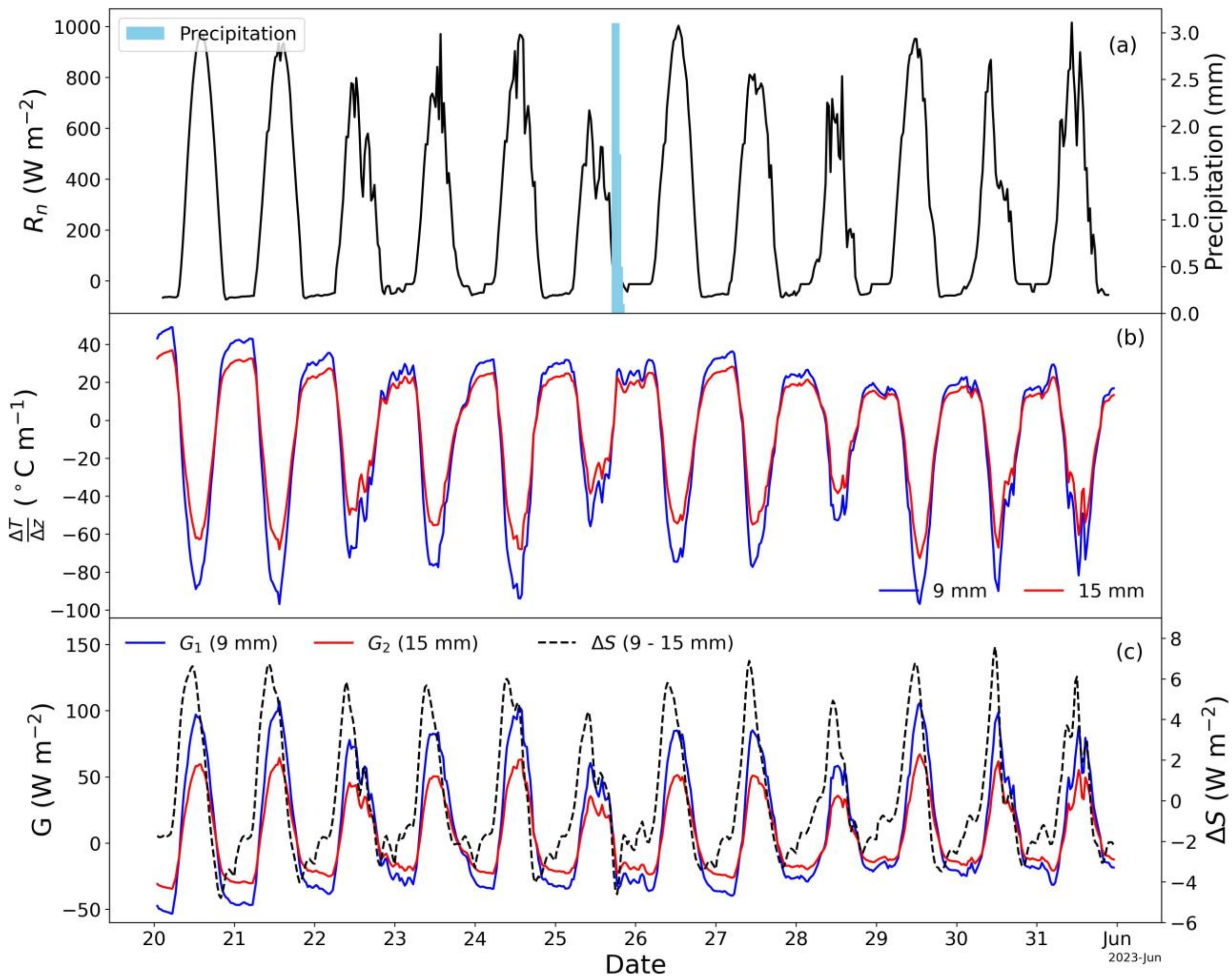

Figure 2-10 (a) Half-hourly net radiation (R_n) values recorded by the net radiometer in the site (b) Soil temperature gradient ($\Delta T/\Delta z$) recorded at two mid-point depths of the shallowest HPP (c) Soil sensible heat flux (G_1 and G_2) and change in sensible heat storage (ΔS) calculated by the shallowest HPP.

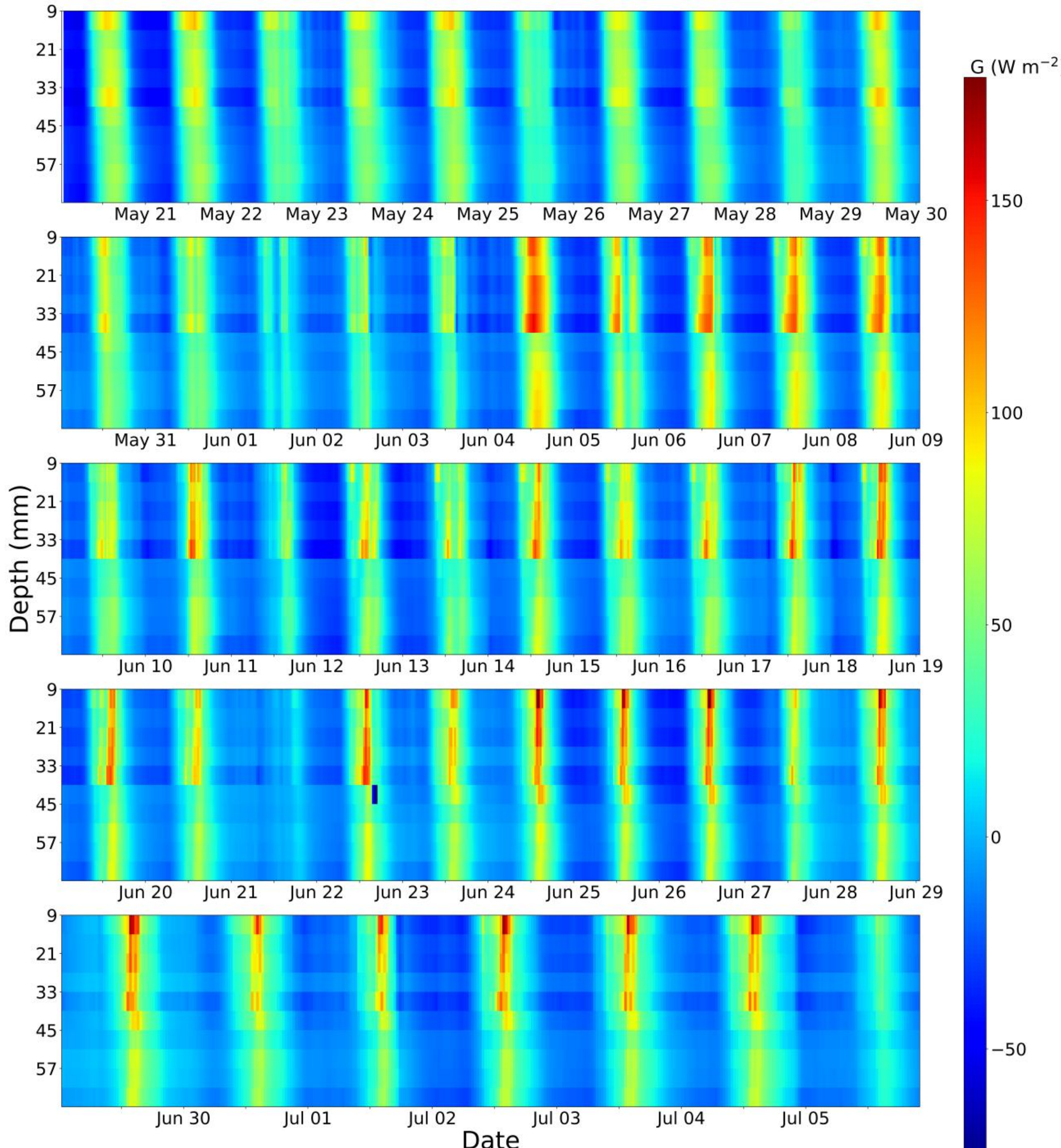

Figure 2-11 Soil sensible heat flux between the top two needles (G_1) recorded by the top nine probes in the soil profile.

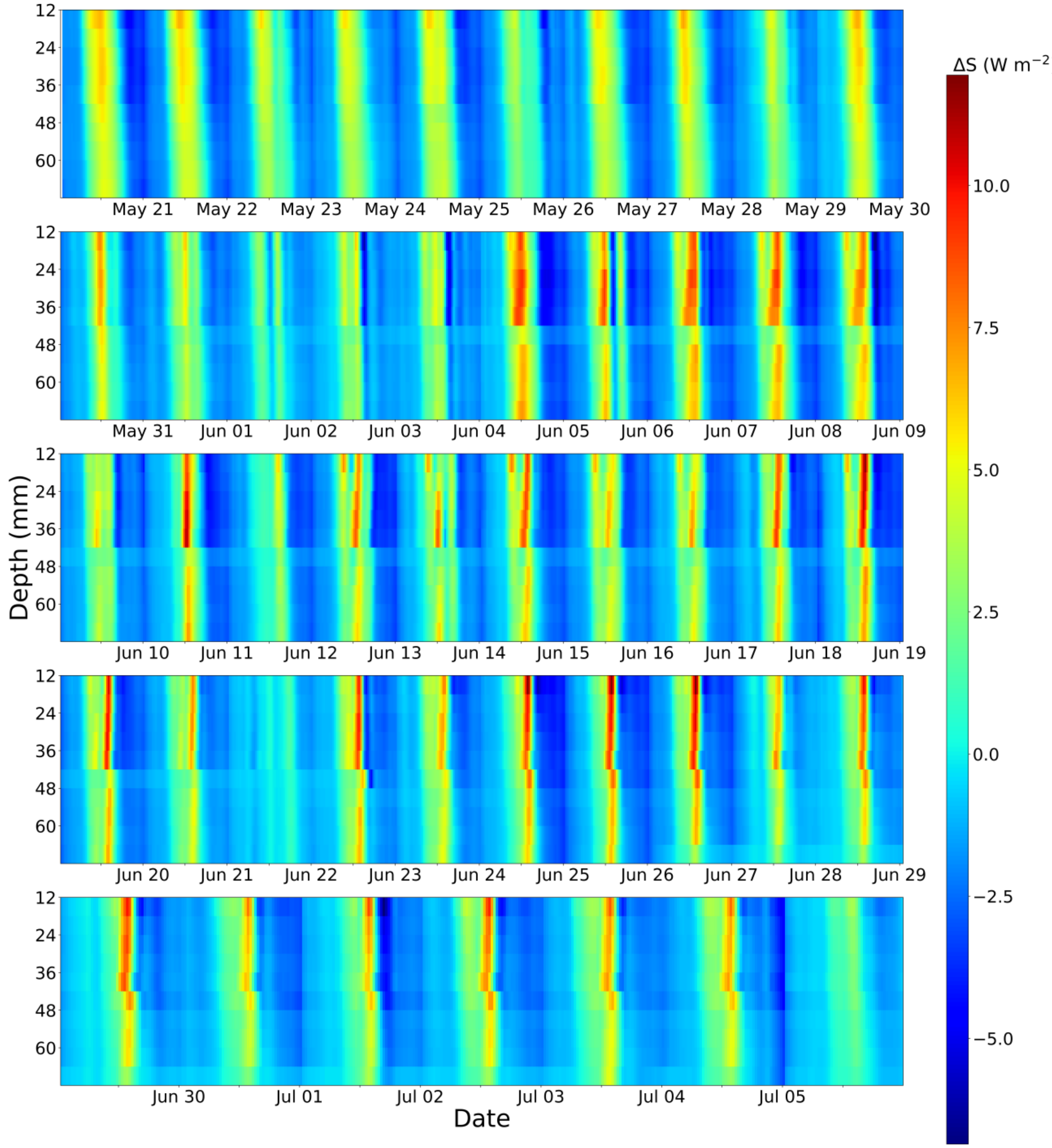

Figure 2-12 Change in heat storage (ΔS) represented by the depth layer between G_1 and G_2 recorded by top nine probes of the soil profile.

Chapter 3 - Quantifying Sub-Surface Soil Water Evaporation using Three-Needle Heat Pulse Probes

3.1 Abstract

Soil evaporation, a key component of the hydrological cycle, accounts for a significant portion of the total precipitation losses in the US Great Plains. However, existing methods for measuring soil evaporation cannot capture the rapidly shifting evaporative front near the soil surface. The soil sensible heat balance (SHB) method, combined with three-needle heat pulse (TNHP) probes, enables high-frequency, continuous monitoring of sub-surface soil evaporation dynamics from fine-scale measurements of soil temperature and thermal properties. The objectives of the study were to a) evaluate the SHB method by comparing its evaporation estimates with independent measurements from the Eddy Covariance (EC) and microlysimeter methods and b) utilize the SHB method to investigate the time and depth patterns of evaporation within soil. TNHP probes were installed at ten depths, beginning just below the soil surface (0.6 cm) and extending to a maximum depth of 7.2 cm. A sensible heat balance was computed by calculating the soil heat flux density at two depths and the change in sensible heat storage between them; the residual in the balance was attributed to latent heat from soil water evaporation. Comparisons of half-hourly SHB estimates with EC data indicated a modest correlation (R^2 = 0.62, root-mean-square error = 0.039 mm h^{-1}). In contrast, the evaporation estimates from the SHB method and microlysimeter showed no correlation (R^2 = 0.002), suggesting that these methods are not compatible for comparison under certain environmental conditions. Time series and depth scale analysis of sub-surface evaporation revealed that shallower depth layers contributed the most to total soil evaporation, with rainfall effects becoming evident only a few days after an event. Evaporation occurred simultaneously at multiple measured depth increments, with a time delay in peak

evaporation at greater depths below the soil surface. Overall, these findings suggest that the SHB method is well-suited for continuous, high-resolution (30 min) monitoring of soil evaporation dynamics in millimeter-scale depth increments.

3.2 Introduction

Evapotranspiration (*ET*), is the second largest component of the hydrological cycle after precipitation (Bastiaanssen et al., 2014; Waring & Running, 2010), consuming over 50% of absorbed net radiation and returning 60% of annual land precipitation to the atmosphere (Zhang et al., 2017, 2019). This combined process of soil evaporation (*E*) and plant transpiration (*T*) is a crucial nexus linking the exchange of carbon and energy between the biosphere and the atmosphere (Fisher et al., 2017; Katul et al., 2012). Since the individual *ET* components have different environmental and biological drivers, their separation is needed to better understand hydrological processes in ecosystems and improve current algorithms used for partitioning *ET* into *E* and *T*. In areas with sparse vegetation, evaporation from the soil surface constitutes a significant proportion of the total *ET* due to considerable areas of exposed soil (Kool et al., 2014; Qiu & Ben-Asher, 2010). Evaporation makes up about 20-40% of global ET (Lawrence et al., 2007; Or et al., 2013) with the majority (65%) originating from soils rather than surface waters in the land (Good et al., 2015).

Soil evaporation is particularly more important in rainfed agriculture of arid and semi-arid regions, where agricultural fields have incomplete ground cover and remain bare for a substantial portion of the growing season (Suleiman & Ritchie, 2003). Several studies around the globe indicate that in agricultural cropping lands, evaporative losses can range from 30-75% of rain during a growing season (Mellouli et al., 2000). Berg & Sheffield, (2019) conducted a global study on ET partitioning using climate models from the Coupled Model Intercomparison Project (CMIP) and found that soil evaporation constituted about 30-40% of the total ET in the U.S. Great Plains. A study using the Agricultural Production Systems sIMulator (APSIM) model to calculate average ET values in a central Iowa corn field revealed that evaporation accounted for 70% of ET from planting to V6 stage of corn (Licht et al., 2017). Considering the significant water loss due to soil evaporation, as highlighted by these aforementioned data, evaporation quantification becomes of paramount importance for reducing these unproductive water losses and enhancing water management practices and agroecosystem productivity (Wagle et al., 2020). Nevertheless, the quantification of E remains challenging.

There are various established methods such as the Bowen ratio energy balance (Fritschen & Fritschen, 2005), eddy covariance (Meyers & Baldocchi, 2015), and water balance techniques (e.g., lysimeter and soil water depletion methods) that have been used for measuring surface soil water evaporation in bare soil (Gong et al., 2020). The eddy covariance (EC) method is a commonly used micrometeorological approach for measuring high-frequency (i.e., 10 Hz or higher) biosphere-atmosphere exchanges of carbon dioxide and water vapor simultaneously at the landscape level (Baldocchi, 2020). Although EC can offer direct and continuous measurements of ET at the field scale, it does not provide direct measurements of ET and CO_2 primary flux components (Wang et al., 2016; Williams et al., 2004; Zhang et al., 2010). So, *E* and *T* have been estimated by partitioning measured ET by the EC approach using methods based, for example, on: underlying water use efficiency (uWUE) (Zhou et al., 2016), gross ecosystem photosynthesis (GEP) (Scott & Biederman, 2017), and separation of ecosystem conductance into soil and canopy conductance (Li et al., 2019). Microlysimeters (ML's) are another widely used technique for measuring soil evaporation due to their simplicity and low cost. ML's are usually made from plastic cylinders that are carefully inserted into the soil to encase an undisturbed soil sample. The bottom of ML is then sealed and soil evaporation is estimated based on changes in total ML's mass in fixed time intervals over a short period of time (~ 3 days). Although this method is relatively simple and provides direct soil evaporation, this measurement is time-consuming, labor-intensive, and ineffective during irrigation or rainfall (Kool et al., 2014). Moreover, MLs cannot provide long-term continuous data because, over time, the ML soil water content starts differing from that of the surrounding soil (Evett et al., 1995). Another major limitation of ML and micrometeorological methods is their inability to accurately measure the highly dynamic near-surface soil evaporation as these approaches are unable to track millimeter-scale soil water movement toward the evaporation zone (Xiao et al., 2011).

The sensible heat balance (SHB) approach estimates evaporation by solving the energy budget for near-surface soil layers (Heitman et al., 2008a). Heitman et al., (2008a,b) applied the SHB method, utilizing a series of heat pulse probes arranged at different depths to estimate subsurface evaporation for bare soil. The applicability of this method has been validated through numerical modeling (Sakai et al., 2011) and experimental studies (Deol et al., 2012; Trautz et al., 2014; Xiao et al., 2011; Xiao et al., 2012). A sensible heat balance is used to determine the amount of latent heat involved in the vaporization of soil water between two measurement depths. The SHB method requires soil temperature gradient measurements to estimate the soil heat flux and soil heat storage for different soil layers. Heat pulse probes can be used to determine soil temperature and thermal properties needed for evaporation estimations using the SHB method (Heitman et al., 2008a; Heitman et al., 2008b) Any residual energy that cannot be accounted for by the change in soil heat flux or storage is attributed to the latent heat flux. More recently, the SHB approach has been extensively applied for continuous soil evaporation quantification across diverse scenarios. For instance, Xiao et al., (2011) used three-needle HP probes, whereas Xiao et al., (2012) and Wang et al., (2017) utilized multi-needle probes to measure soil water evaporation for bare soil. Xiao et al., (2014) evaluated the applicability of the SHB method under a crop (maize) canopy cover when the soil was drying, and Xiao et al., (2016) evaluated the same during consecutive wetting-drying periods. Wang et al., (2015) determined soil evaporation in a sparse stand of Chinese willow (*Salix matsudana*) and validated SHB evaporation against microlysimeter evaporation. Deol et al., (2012) quantified nonisothermal soil evaporation under laboratory conditions and Trautz et al., (2014) investigated the applicability of the SHB approach by comparing laboratory experimental data with analytical methods. A major drawback of the use of three-needle heat pulse probes to estimate soil evaporation using the SHB method is their inability to provide evaporation data from the soil layer extending from the soil surface down to the midpoint between the top and middle needle of the shallowest heat pulse probe (Xiao et al., 2012). Consequently, they are less effective immediately after wetting events, when evaporation (Stage 1) mainly occurs at or near the soil surface (Heitman et al., 2020; Kool et al., 2014). Therefore, efforts to improve the evaporation estimation such as using an 11-needle probe with closer spacing near the soil surface (Xiao et al., 2012) and modifying the SHB method to account for stage 1 evaporation (Xiao et al., 2014) have also been made. A significant problem that remains is in the employment of the heat transfer model being used for estimating soil thermal properties required to solve the sensible heat balance equation.

To our knowledge, no studies have reported SHB-estimated evaporation experiments using the identical-cylindrical-perfect-conductors (ICPC) model. Instead, all previous studies have relied on the infinite line source (ILS) model to derive soil thermal properties. However, the ILS model assumes finite heat capacity and probe dimensions, which conflict with the design of modern probes being used. The ICPC model enhances heat transport solutions by incorporating probe heat capacity and radius (Kamai et al., 2015).

In this study, we used the SHB method combined with three-needle heat pulse probes and the ICPC model, to accurately quantify the components of the heat balance and measure continuous, high-frequency sub-surface evaporation over both depth and time in the field. The objectives of this study were to: 1) compare 30-min E estimates from the SHB method with the ones estimated using the EC approach, 2) compare SHB estimated daily E with those provided by microlysimeters and 3) evaluate near-surface soil evaporation spatial and temporal dynamics using the SHB method with heat pulse probes.

3.3 Theory

3.3.1 Soil Sensible Heat Balance Method

Gardner & Hanks, (1966) proposed a sensible heat balance equation for estimating evaporation occurring within the soil, by assuming that the heat flow through the soil layer is one-dimensional:

$$(G_1 - G_2) - \Delta S = LE \qquad [3.1]$$

where G_1 and G_2 (W m^{-2}) are soil sensible heat fluxes at depths 1 and 2, respectively; ΔS (W m^{-2}) is the change in soil sensible heat storage between depths 1 and 2 (Section 2.3.1); L (J m^{-3}) is the latent heat of vaporization of water; and E (m s^{-1}) is the evaporation rate.

Measurements of soil temperature and thermal properties required for analyzing the heat balance are provided by heat pulse probes and the ICPC model (Section 2.4.3.3).

3.4 Materials and Methods

3.4.1 Evaporation Measurements in a Corn Field

3.4.1.1 Site description

Soil evaporation measurements were conducted in two field experiments. The first experiment was carried out at a commercial corn field in Gypsum, Kansas (38.7140º N, 97.4235º W) from May 20 to July 05, 2023. The soil of the experimental site is mapped as Hord silt loam. Particle size analysis, determined using the hydrometer method (Gavlak et al., 2005), indicated the proportion of sand, silt and clay were: 18%, 58% and 24%, respectively. The average soil bulk density (ρb) was determined to be 1.33 (g cm^{-3}), which was estimated from six soil cores collected at 0 - 7.5 cm depth using ring samplers (7.62-cm diameter and 7.5-cm long).

3.4.1.2 Heat pulse and soil temperature measurement

Heat pulse probes were installed in between the rows of corn nine days after sowing. Ten HP probes were installed at ten depths beginning just below the soil surface (0.6 cm) and extending to a maximum depth of 7.2 cm. The probe installation and data acquisition for heat pulse and soil temperature measurement were same as those of the heat flux measurement described in Chapter 2.

3.4.1.3 Eddy covariance measurements

In addition to the HP probes set up, an EC measurement station was located 4 m from the HP instrumentation. Fluxes of CO_2 and H_2O were measured using the eddy covariance (EC) technique. The three orthogonal components of wind velocity and temperature were recorded with a sonic anemometer (CSAT3, Campbell Scientific, Inc., Logan, UT). An open-path CO_2/H_2O infrared gas analyzer (LI-7500RS, LI-COR, Lincoln, NE) was used to measure carbon dioxide and water vapor concentrations. The sonic anemometer and open-path gas analyzer were mounted on a tower 2.7 m above the ground. Air temperature and relative humidity were measured using a standard air temperature and moisture probe (HMP 50, Campbell Scientific, Inc., Logan, UT). The signals from the sonic anemometer, and the open-path gas analyzer were acquired at a rate of 20 Hz using a SmartFlux 2 system (LICOR). The half-hourly fluxes were calculated on site by the SmartFlux 2 system using the software EddyPro (EddyPro 7.0.9, LI-COR).

Net radiation (R_n) was measured with a four-component net radiometer (NR01, HukselfluxUSA, Inc., Center Moriches, NY) at 1-m above the ground. Precipitation (P) was measured using a tipping bucket rain gauge (Model No. TRP525I, Texas Electronics Inc., Dallas, TX). The sensors were scanned at 10-s intervals using a datalogger (CR3000, Campbell Sci.) and average R_n and total P were computed for 30-min intervals.

3.4.1.4 Flux gap filling

Flux data gaps were caused by equipment failure and measurement over periods when atmospheric conditions were not suitable for flux measurements. These gaps were filled using the well-established ReddyProcWeb online tool from the Max Planck Institute for Biogeochemistry (Wutzler et al., 2018) utilizing flux and meteorological data. Half-hourly values of net CO_2 ecosystem exchange, latent heat flux, shortwave incoming radiation (Rg), air temperature (Tair), relative humidity (rH), and vapor pressure deficit (VPD) collected at the site were used for gap filling. When these meteorological variables were not available at the site, we utilized data from a nearby Kansas Mesonet station for gap filling fluxes.

3.4.2 Microlysimeter and SHB Methods Soil Evaporation Comparisons

3.4.2.1 Site description

To evaluate the SHB-estimated soil evaporation, daily estimates of water loss from the soil was measured using conventional bottom-sealed microlysimeters. The study was conducted in a research plot of Manhattan Plant Materials Center (KSPMC), USDA, NRCS (39.1872º N, 96.5902º W), Manhattan, Kansas from October 25 to November 23, 2024. From here on, the site will be referred to as the Ashland site. The soil at the site is mapped as Belvue silt loam, rarely flooded. This plot is part of a long-term tillage study so the soil has been regularly tilled for many years and kept bare by spraying herbicides for weed control.

Net radiation and precipitation were measured as described in Section 3.4.1.3.

3.4.2.2 Heat pulse and soil temperature measurement

Before ML and equipment installation, the soil was tilled using a rotary tiller, then leveled and compacted. An 18 m^2 area was designated for the study and cleared of all vegetation and surface residue to maintain a bare soil condition. HP probes were carefully inserted into the undisturbed soil sidewall at the center of the selected plot. The heat pulse and temperature measurements were identical to measurements described in Section 2.4.3.2.

3.4.2.3 Soil evaporation from SHB Method

Soil sensible heat balance components were determined to solve the sensible heat balance equation for estimating sub-surface evaporation from a soil layer. Soil sensible heat flux (G) was computed as described in Section 2.3.1. Sakai et al., (2011) found through numerical analysis that the estimation of E was more influenced by λ than by C, and that, overall, ΔS played a smaller role in Eq. [3.1] compared to G. As the conduction component of heat flux is the dominant process at the evaporation front, the computational accuracy of evaporation rate can be improved further using depth-dependent conductivity (λ_n) for determining G instead of a space averaged conductivity (λ). Therefore, unlike other studies (Heitman et al., 2008a; Heitman et al., 2008b; Xiao et al., 2012), we used locally determined λ between each heater needle and the adjacent thermistor needle instead of averaging λ across both sides of the heater needle.

Calculation of ΔS (W m^{-2}) was identical to the method described in Section in 2.3.1. The soil temperature time derivative (dT/dt) required for ΔS (W m^{-2}) was also calculated as described in Section 2.4.3.4. After computing G_1, G_2, and ΔS, equation [3.1] was used to determine LE. Values for L were calculated from (Forsythe, 1954)

$$L = 2.49463 \times 10^9 - 2.247 \times 10^6\ T_m \qquad [3.2]$$

where T_m (° C) is the mean temperature for a given depth layer and time step. A positive value of LE indicates water evaporated in the calculated soil layer, and a negative value of LE indicates water vapor condensed in the calculated layer. Having values for G, ΔS, and L, E was calculated from Eq. [3.1].

3.4.2.4 Soil evaporation from microlysimeters

Soil evaporation measurements were also conducted using MLs. The MLs were made from a polyvinyl chloride (PVC) pipe (i.d. = 10 cm). The PVC pipe was cut into 12-cm segments with a beveled bottom edge to facilitate penetration into the soil. A total of 16 MLs were installed within the experimental plot, with four placed on each side of the centrally located heat pulse probes. To ensure comprehensive spatial representation, each set of four MLs included two positioned near the HP probes and two near the plot’s edge. This arrangement was designed to capture variability across the field plot effectively. MLs were installed with the aid of a wooden block and a nylon mallet, ensuring that the top of the ML remained level with the soil surface. The installation process can result in minor soil disturbances, which can affect our evaporation measurements. Rainfall restores soil surface conditions affected by installation vibrations, and helps seal small gaps between the ML walls and the surrounding soil (Da Rocha et al., 2022). Therefore, installation was completed approximately three weeks before measurements, which allowed several wetting and drying cycles in the soil before their use.

On selected days, when the weather forecast indicated low precipitation probability for the next three days, one ML from each side of the probe location was carefully excavated using a shovel to minimize disturbance to the soil column inside the ML. The excess soil on the ML bottom was carefully removed to form a flat surface, which was sealed with a thin nylon film (GLAD PRESS’NSEAL) and duct tape to eliminate drainage losses and to ensure the integrity of the soil column inside the ML. The sealed MLs were then weighed in the field with a portable balance (±1 g, Model V11P6, Ohaus Corp., Parsippany, NJ) and returned to their original position, with surrounding soil carefully repacked so that the MLs were flush with the soil surface. After 24 hours, the sealed MLs were again removed from the surrounding soil and reweighed to determine their change in mass. Each ML was used for no more than four days so that the soil moisture conditions inside the ML remained similar to that of the surrounding soil (Evett et al., 1995). The total mass change was attributed to loss of water via net evaporation. For each measurement day, soil evaporation rate was determined as the average soil evaporation rate of the four MLs. Soil evaporation (E, mm d^{-1}) was calculated as follows (Wang and Wang, 2017):

$$E = 10 * \frac{\Delta W/\rho}{\pi\left(\frac{D}{2}\right)^2} \qquad [3.3]$$

where the factor 10 in the equation is to convert the cm to mm, ΔW (g) is the change in mass of the ML between two measurements, ρ is the density of water (1.0 g cm^{-3}), and D is the diameter of the ML (cm).

The SHB approach measures in situ evaporation at various depth intervals beneath the soil surface, whereas microlysimeters only offer information on the overall net evaporation. To establish a basis for comparison, we aggregated the daily values from Eq. [3.1] across all measured depth increments to estimate the total daily evaporation and then compared to the total daily evaporation measured by microlysimeters.

3.5 Results and Discussion

3.5.1 Temporal Dynamics of Soil Heat Fluxes and Evaporation

Fig. 3-1 presents a time-series of R_n, soil sensible heat fluxes and heat storage, and evaporation recorded by the topmost probe in the soil profile during eight consecutive days of the field study at the Gypsum site. R_n values ranged from about -67 W m^{-2} to 1015 W m^{-2}, with daily maximum values surpassing 800 W m^{-2} on most days (Fig. 3-1a). The daily variation in R_n can be attributed to the changes in incoming solar radiation caused by cloud cover. The daily maximum sensible heat fluxes at 9 mm (G_9) ranged from 58 to 105 Wm^{-2}, and those at 15 mm were between 35 and 67 Wm^{-2} (Fig. 3-1b). The diurnal variation in G can be very well explained by the variation in R_n, suggesting that the net radiation was the major driver for heat flux. Daily maximum ΔS values were much smaller than G estimates with values ranged from 7.5 to 4 Wm^{-2} (Fig. 3-1b). Both the field measurement conducted by Heitman et al., (2008b) and the numerical simulation study by Sakai et al., (2011) revealed that the change in ΔS was significantly smaller compared to the change by conduction heat flux. These findings align closely with our results. As the amount of heat partitioned to ΔS throughout the measured period remained consistently small, the difference between the measured heat flux at 9-mm and 15-mm appreciably exceeded ΔS, revealing the occurrence of evaporation at the 9 - 15 mm layer (Eq. 3.1). Evaporation from the 9-15 mm soil layer (Fig. 3-1c) was very well coupled with net radiation, indicating a major influence of soil temperature gradient at that shallow layer. Wang et al., (2021) partitioned *ET* by measuring *E* with *HP* probes and *T* with sap flow gauges and reported similar findings where the shape of the *E* curve resembled that of the net radiation.

3.5.2 Comparing SHB Half-Hour Evaporation to Eddy Covariance Estimate

Figure 3-2 illustrates the comparison between total evaporation from ten soil layers obtained using the SHB method and the EC method at the Gypsum site. The SHB method recorded evaporation values ranging from -0.04 to 0.14 mm h^{-1}, while the EC method recorded values between -0.04 and 0.36 mm h^{-1}. The figure reveals that the flux tower consistently measured higher evaporation estimates compared to the heat pulse probes. This discrepancy becomes even more pronounced the day after rainfall, when the flux tower records significantly higher evaporation rates than the heat pulse probes. The sharp increase in evaporation recorded by the flux tower on May 26 could be due to the loss of moisture retained by crop residues on the soil surface, which evaporated the following day when sufficient energy became available. Since the design of the probes used in our experiment limited the detection of evaporation occurring above the 9 mm soil depth, no increase in SHB evaporation from the heat pulse probe was observed until May 29. Only three days after the rainfall, evaporation from HPP increased to align well with E from the flux tower. This increase in evaporation indicated the progression of the evaporation zone into deeper depths, which could have been captured by the HPPs. Negative values of E (i.e., $E < 0$) were also observed from the heat balance, which suggested condensation. Limited methods are available for temporal comparison of fine-scale soil water evaporation measurements. While the EC method does not measure evaporation separately when vegetation is actively growing, just after germination when the leaf area index is still very small, the total ET from the flux tower can be assumed to be equal to the soil evaporation, thus enabling comparisons between fluxes measurements obtained from the SHB and EC approaches.

We conducted a regression analysis to compare the half-hourly evaporation estimates from the two methods excluding the measurements taken the day following rainfall. Here we only included direct measurements by the two methods; we excluded EC flux data estimated using the gap filling approach. The regression analysis as shown in Figure 3-3 indicated good correlation between the heat balance and the eddy covariance estimates with $R^2 = 0.62$ and root-mean-square-error (RMSE) = 0.039 mm h^{-1} recorded for 10 days of measurement. We hypothesize the difference between EC and SHB approach estimates could have been caused by: 1) differences in the spatial area measured by the two methods, 2) the contributions to total evaporation from crop residue and the top 0-0.9 mm soil layer that were not measured by the SHB method and 3) potential contribution of transpiration from small corn plants to the EC measured fluxes.

The HPPs measure high-resolution localized evaporation, with a footprint on the order of < 0.1 m^2, whereas direct EC measurements of evaporation can have a footprint on the order of hundreds of square meters. So, it is likely that the tower sampled areas of the field with different evaporation rates than the small area measured by the SHB method. The inability of our probe to capture evaporation from the top 9 mm of soil could be another reason for the difference in estimates. Moreover, even though we considered our experimental site to be bare soil, the small corn plants might have still transpired by drawing water from the uppermost soil layer, which could have been detected by the flux tower. Despite these differences, the evaporation temporal pattern from both the methods aligned well, which demonstrate the potential of the heat balance method for fine time (30 min) and depth (mm) scale measurements of evaporation.

3.5.3 Comparing SHB and Microlysimeter Daily Evaporation Estimates

ML evaporation estimates were collected over eight days during three sampling campaigns. The comparison of daily evaporation values derived from the SHB method and those measured by ML at the Ashland site is shown in Figure 3-4. Daily evaporation from the microlysimeters ranged from 3.69 to 0.98 mm d^{-1}, with an average daily coefficient of variation of 22% among replicates. In general, evaporation was greatest on the first day of measurement, the day following rainfall, and gradually declined on subsequent days. The lowest evaporation rates were observed on the final day of each sampling campaign. SHB-derived evaporation estimates ranged between 3.39 and 2.18 mm d^{-1}, with the largest discrepancy between the two methods i.e. 2.2 mm d^{-1} occurring on the last day of the third sampling campaign. Overall, the average difference between the two approaches was 1.18 mm d^{-1}.

Heitman et al., (2008b) compared evaporation from independent estimates (microlysimeters and the Bowen ratio method) with SHB measurements. Their findings indicated a strong correlation (R^2 = 0.96) with an RMSE of 0.20 mm, though their analysis excluded measurements from the first three days after rainfall. In contrast, our study incorporated these early post-rainfall measurements, which may have contributed to the larger discrepancies observed. To overcome this issue, an 11-needle HPP design developed by Xiao et al., (2012) can be used to minimize the 'undetectable zone'. Another solution could be to use a modified SHB approach, as proposed by Xiao et al., (2014), that accounts for Stage 1 evaporation. Their modified SHB improved evaporation estimates under moist soil conditions following rainfall. The observed discrepancies between the two methods in our study are most likely due to the inability of our probes to detect Stage 1 and the 'undetectable zone' *E*. This assumption is validated by Deol et al., (2014) who examined the inception and magnitude of subsurface *E* in a wet loamy sand soil and reported that the onset of subsurface evaporation coincided with the beginning of Stage 2 evaporation.

Figure 3-4 also indicates that, within each sampling campaign, microlysimeter evaporation consistently declined in response to decreasing soil moisture, whereas SHB-derived evaporation either remained stable or increased after the first measurement day. This divergence in trends may be attributed to fundamental differences in the measurement principles of each method. Since microlysimeters are sealed at the bottom, they prevent upward water movement, potentially limiting evaporation. In contrast, the SHB method allows for unrestricted water movement, enabling deeper soil layers to contribute to evaporation through capillary rise. As a result, SHB-derived evaporation may persist even as surface soil moisture declines.

The correlation between SHB and microlysimeter evaporation estimates was poor (R^2 = 0.002), likely due to differences in their measurement conditions. Future research should explore modifications to the SHB technique to expand its applicability across a wider range of environmental conditions.

3.5.4 Sub-Surface Evaporation Measurements from SHB Method

The depth-wise variation in evaporation (Figure 3-5) demonstrates that the top layer contributed the most to the total evaporation with a peak evaporation rate as high as 0.056 mm h^{-1}. Soil evaporation generally decreased with depth; however, an anomaly can be observed at 36 mm depth, where consistently higher evaporation rate than from depths closer to the soil surface, i.e., 24 and 30 mm, was observed. This could be due to the spatial heterogeneity in the surface residue cover and thermal properties of soil. Evaporation from depths 24, 30, and 36 mm begins to rise a few days following the rainfall, with their magnitude and pattern aligning perfectly on May 30, four days after the rain. This increase in the magnitude starting May 29 indicates that the evaporation zone moved below the 12 mm depth to deeper depths. As the surface soil continued to dry on subsequent days after rainfall and the depth of the dry soil layer increased, the evaporation rate in the deeper layer began to increase, which is also confirmed by the close alignment of evaporation patterns from the SHB and EC methods on May 29 (Fig. 3-2). Although the evaporation rate from the 12 mm did not change significantly, the increase in evaporation from depths below it contributed to the increase of the total evaporation due to the progression of the evaporation zone in the deeper profile. A time lag (3 hr) in the occurrence of daily evaporation peaks can also be observed at 30 mm depth, which after the rain, starts matching with the daily peaks at other depths. This observation is consistent with the findings of Heitman et al., (2008a), that demonstrated a time lag for peak evaporation rates between depth increments. Although there is a lag in evaporation peaks, the magnitude seems higher than at 24 mm.

A larger time lag (16 hr) in daily evaporation peaks was observed at depths 48 mm and 60 mm. However, at 60 mm, evaporation reaches its peak earlier than 48 mm depth. An inconsistency in daily peak occurrence was observed on May 29, where evaporation peak at 48 mm occurred during the same time as other upper depths. This suggests that the 48-mm depth also contributed to the total evaporation from the profile as other shallower depths. Negative values of E indicate condensation, which for shallower depths, was mostly observed during nighttime. Such observation was also made by Heitman et al., (2008a) which reported condensation from soil layer as shallow as 3-8 mm. Similar findings were observed in sandy loam soil in China where an 11-needle heat pulse probe captured negative E rates from soil depths 1.5 - 48 mm (Xiao et al., 2012). Nevertheless, condensation can occur even during daytime for deeper depths due to the time lag in heat conduction in deeper layers. No significant evaporation was observed at soil layers deeper than 42 mm. This observation agrees with that of Lu et al., (2018) and Xiao et al., (2012) in which water evaporation occurred mostly at upper soil depth.

Figure 3-6 illustrates the sub-surface evaporation rates throughout the entire measurement period i.e. May 20 to July 5. The temporal and spatial scale evaporation dynamics revealed a similar pattern as seen in Figure 3-5 Evaporation rates seemed to increase later during the period, with the maximum E from 12 mm reaching as high as 0.09 mm h^{-1}. Consistent time lags in evaporation peaks were observed at greater depths. A significant observation was that even at the deepest soil profile, condensation was not observed throughout the 24 hr cycle. This suggests that, though at a reduced rate, evaporation continues to occur at deeper soil depths. The spatial scale evaporation dynamics as shown in Fig. 3-6 proves the ability of the SHB approach to provide soil water evaporation information at a localized, millimeter-scale as a function of depth and time.

3.5.5 Total Soil Evaporation During the Experimental Period

Figure 3-7 presents the total evaporation from the 9 to 63 mm soil profile at the Gypsum site over 46 days, spanning from corn emergence to full canopy closure. The time series reveals a strong relationship between evaporation and net radiation, with lower evaporation occurring on days when net radiation is reduced. This pattern underscores that the SHB is capable of capturing high frequency (<1 h) temporal dynamics of soil evaporation. Evaporation typically peaked around midday, when energy availability was at its highest, and declined thereafter. Multiple rainfall events were observed throughout the study period, varying in magnitude. Following these rain events, evaporation tended to increase, driven by enhanced soil moisture availability.

In the early season (late May to early June), total evaporation rates remained relatively low but exhibited a gradual upward trend. Even though there was enough energy available, the lower evaporation rates could be the result of dry soil during the start of the experiment. The rainfall on May 25 seemed to have an increasing effect on total evaporation, which could be seen on May 29. As the season progressed, evaporation increased at an accelerating rate, with peak values becoming more pronounced, reflecting a broader seasonal warming trend. By mid to late June, evaporation reached its highest levels, likely due to increased net radiation and greater energy availability. Additionally, intermittent rain events during this period contributed to elevated evaporation rates by replenishing soil moisture. However, toward the end of June, evaporation begins to decline, coinciding with the closure of the corn canopy, which limits direct solar radiation reaching the soil surface.

Despite this reduction, evaporation remained relatively high from late June to early July. We suspect the increased air temperature (data not shown) to be the reason for increased evaporation rate, sustaining soil evaporation even in the absence of direct sunlight. Another key observation is that condensation remains minimal, if not absent, during July. This may be attributed to a combination of high soil temperatures limiting vapor saturation, increased longwave radiation emitted by the canopy, and sustained evaporation preventing moisture accumulation.

3.6 Conclusions

The results demonstrated that when the net sensible heat flux for a soil layer exceeded ΔS for the layer, it resulted in the occurrence of sub-surface evaporation, and net radiation was a major factor influencing soil evaporation. Comparison of half-hourly evaporation estimates from the EC and SHB methods revealed some discrepancies, with the EC method consistently reporting higher values. This suggests a limitation of our probes in capturing evaporation from the uppermost 9 mm of soil, where heat balance calculations are not feasible, leading to an underestimation of total subsurface evaporation. Differences in measurements between the two methods were also likely due to variation in measurement scale, as heat pulse probes did not capture the full extent of field variability. Despite these differences, both methods exhibited similar evaporation patterns, with peak evaporation rates matching precisely three days after rainfall. Regression analysis between the two methods demonstrated a reasonably strong correlation, with an R^2 of 0.62 and an RMSE of 0.039 mm h^{-1}.

The comparison of daily evaporation estimates from the SHB and microlysimeter methods indicated that that SHB- derived evaporation was consistently higher, with a maximum difference of 2.2 mm d^{-1} over the eight-day measurement period. Unlike SHB, which showed increasing rates over consecutive days, evaporation from the microlysimeter steadily declined during the drying period. This decreasing trend was likely due to restricted upward water movement, as microlysimeters are sealed at the bottom, preventing capillary rise from deeper soil layers.

Depth-wise analysis of subsurface evaporation revealed that evaporation rates were highest near the surface and progressively declined with depth. Additionally, time lags in daily peak evaporation were observed at certain depths. Although rainfall did not immediately influence evaporation, its effects became evident at shallower depths after a few days.

Overall, the findings underscore the strong potential of the SHB approach for high-frequency subsurface evaporation estimation. These insights highlight an opportunity to integrate SHB-derived evaporation estimates into existing soil evaporation models and improve ET partitioning during wetting-drying cycles.

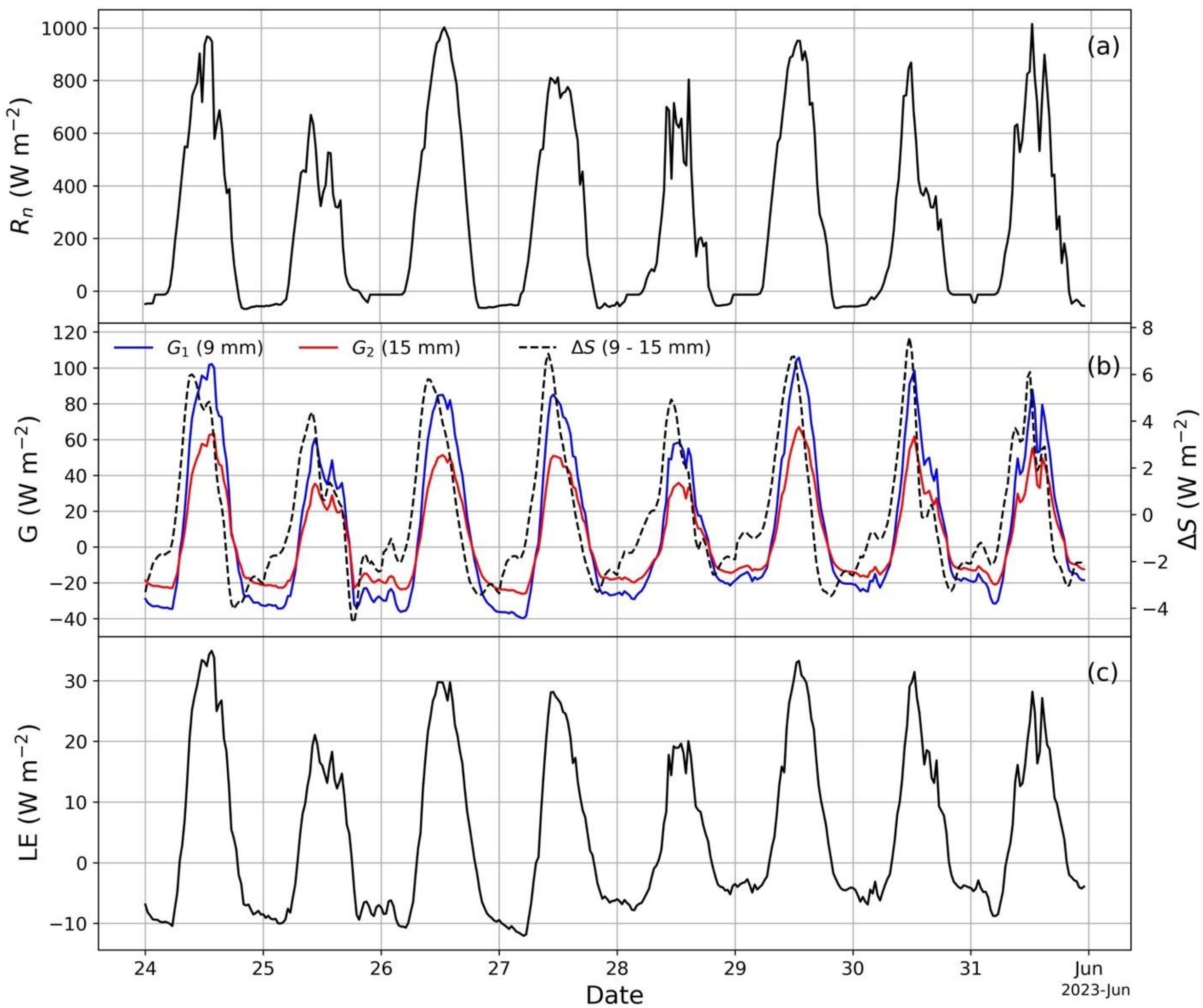

Figure 3-1 Half-hour values of (a) net radiation (R_n), (b) soil sensible heat fluxes (G) and heat storage (ΔS), and (c) soil evaporation from the topmost probe in the profile in Gypsum site.

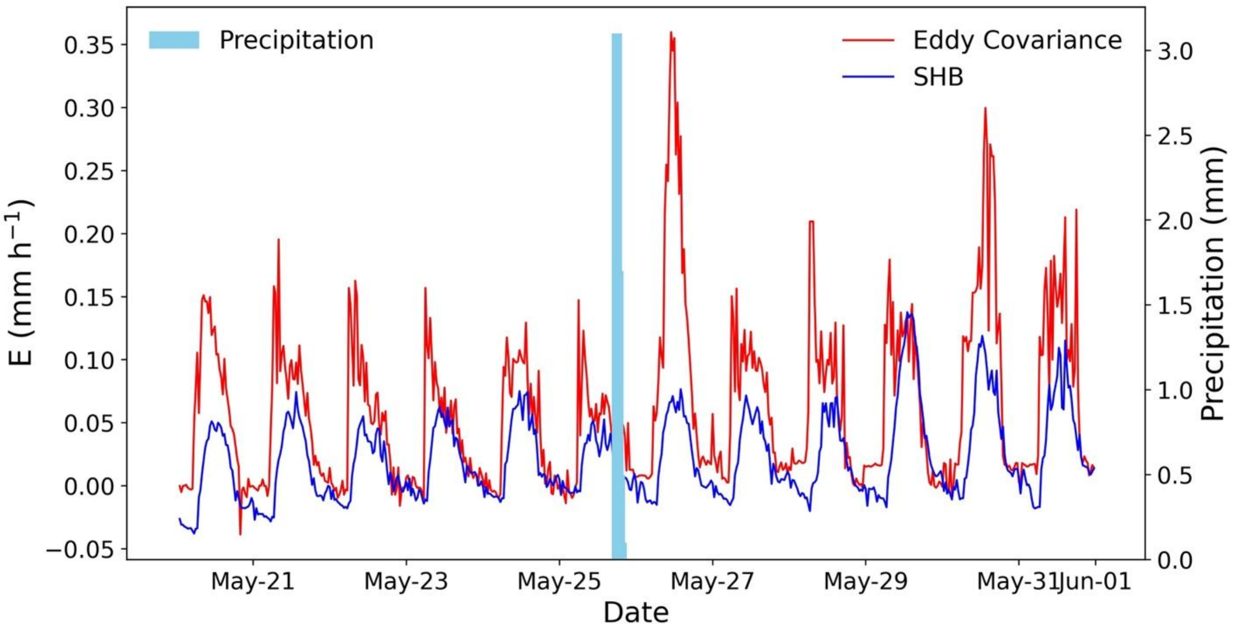

Figure 3-2 Comparison of half-hour evaporation values from the Sensible Heat Balance (SHB) and Eddy Covariance (EC) methods. Data were collected from the inter-rows of corn plants at the Gypsum site. The soil surface also had some residue cover.

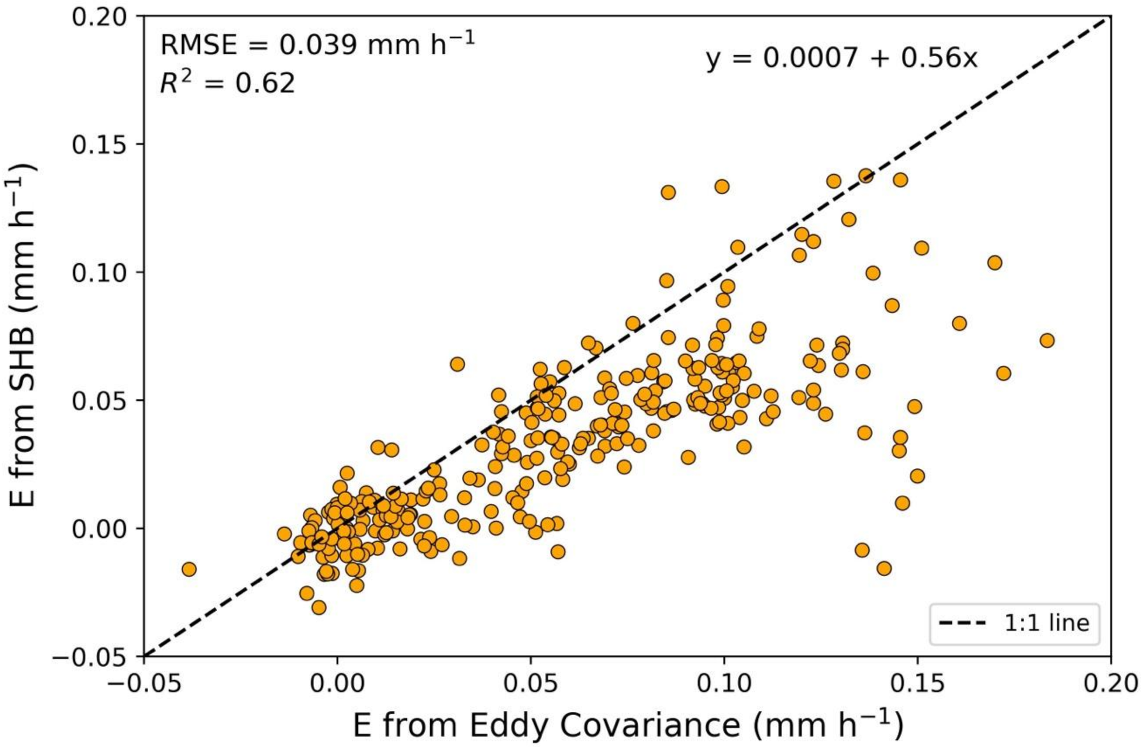

Figure 3-3 Regression analysis of evaporation obtained using SHB and EC methods at the Gypsum site. Data from the day following rainfall (May 26) are excluded.

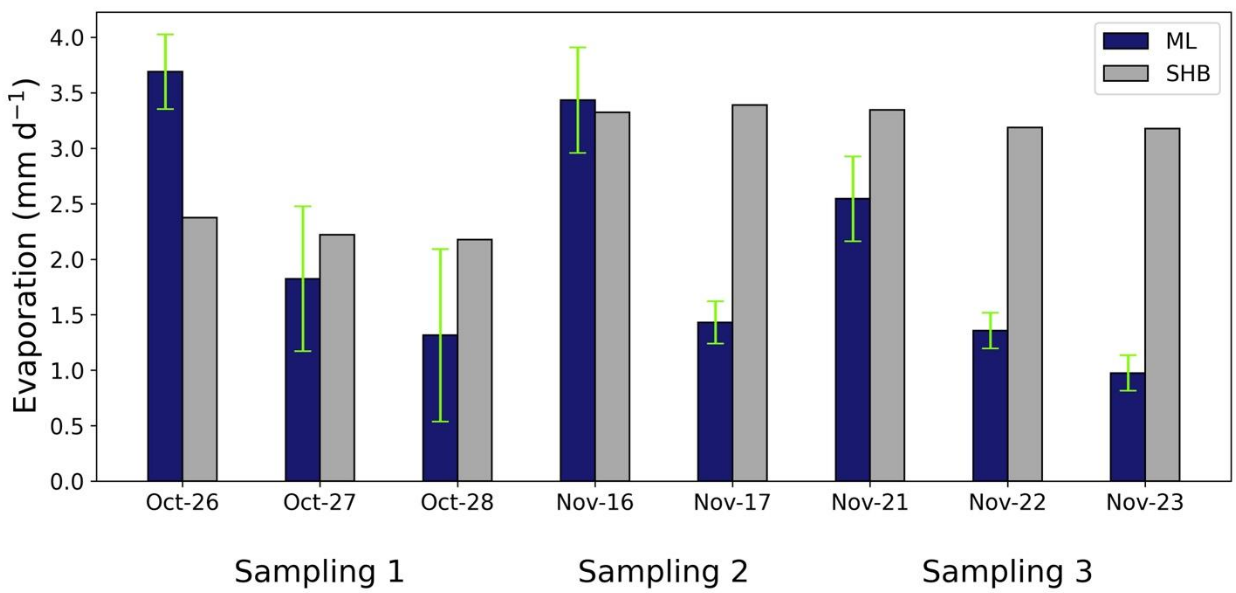

Figure 3-4 Daily values of soil evaporation derived from the sensible heat balance (SHB) method and measured by microlysimeters in bare soil conditions (Ashland site). Error bars represent the standard deviation of microlysimeters.

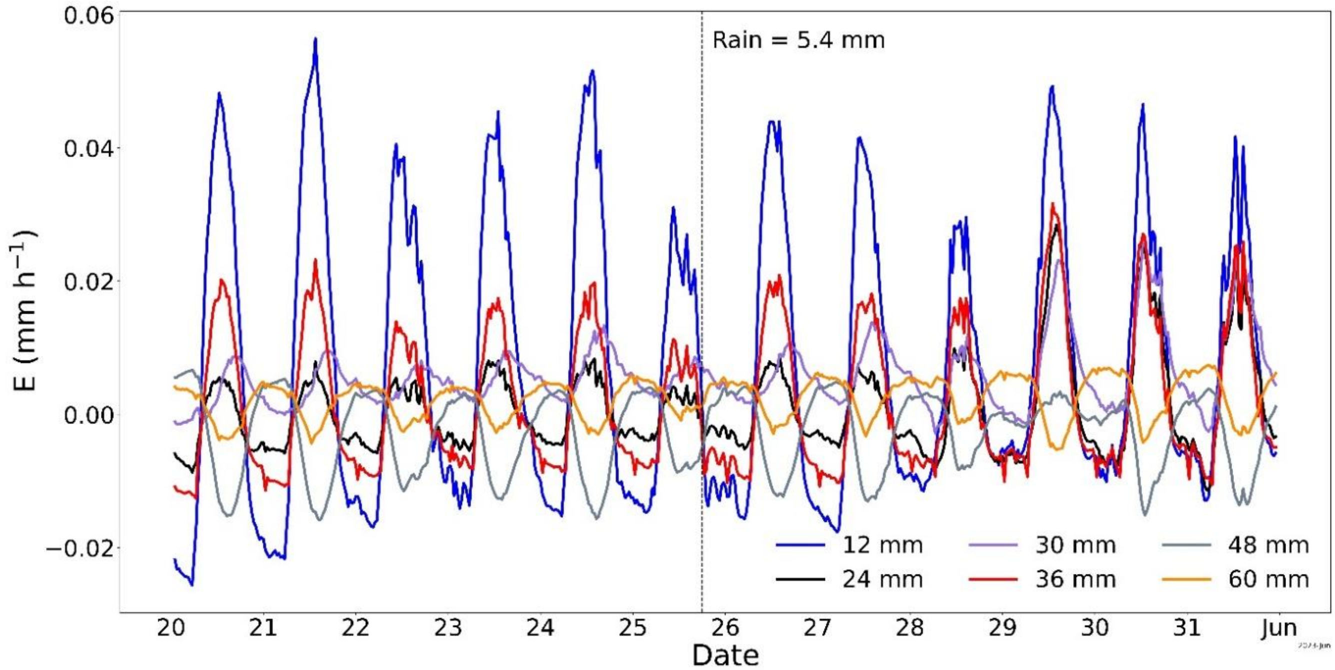

Figure 3-5 Sub-surface soil evaporation rate at different depths of the soil profile at the Gypsum site.

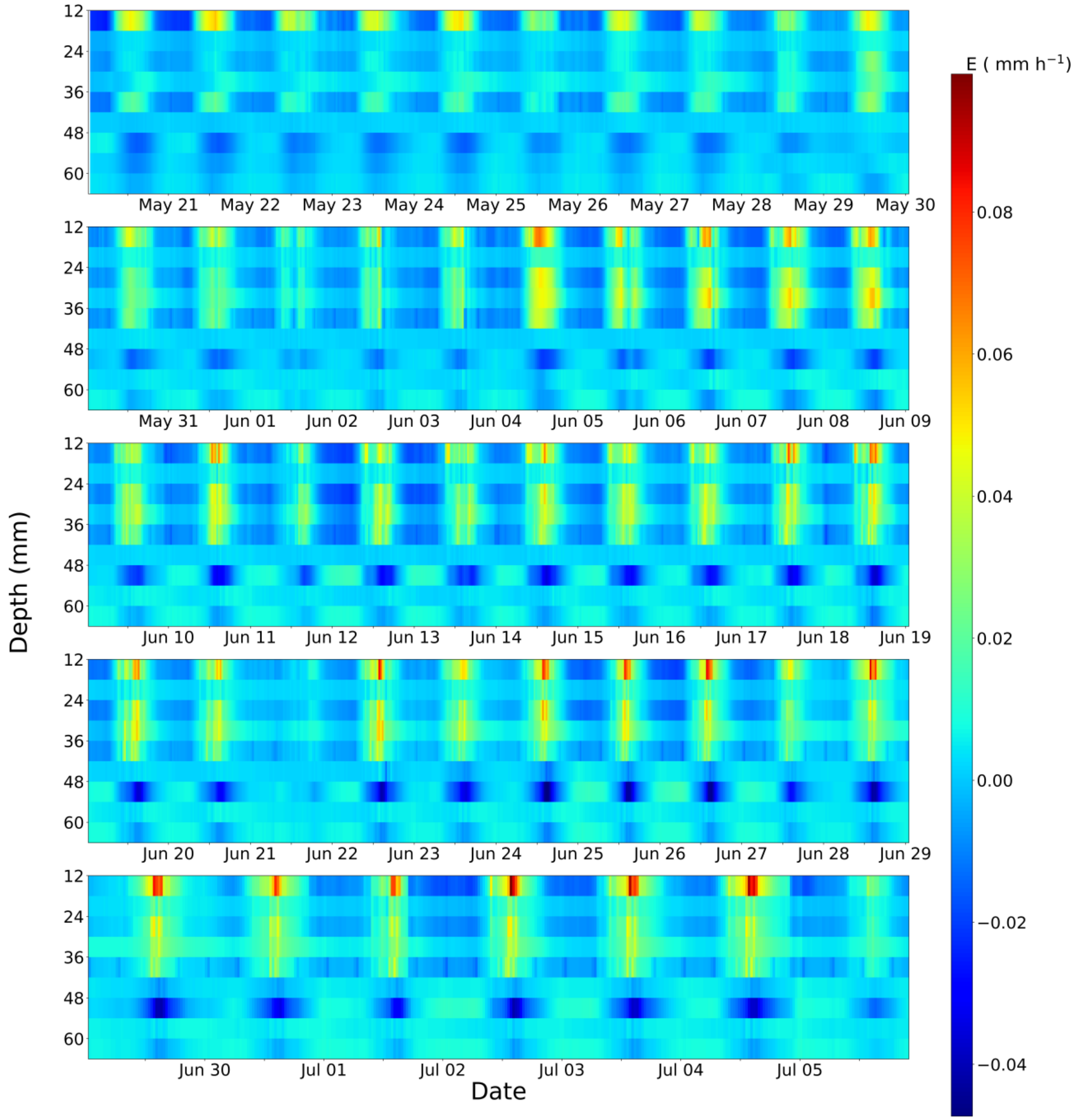

Figure 3-6 Temporal and spatial sub-surface evaporation dynamics from the corn field at the Gypsum site for the total experimental period.

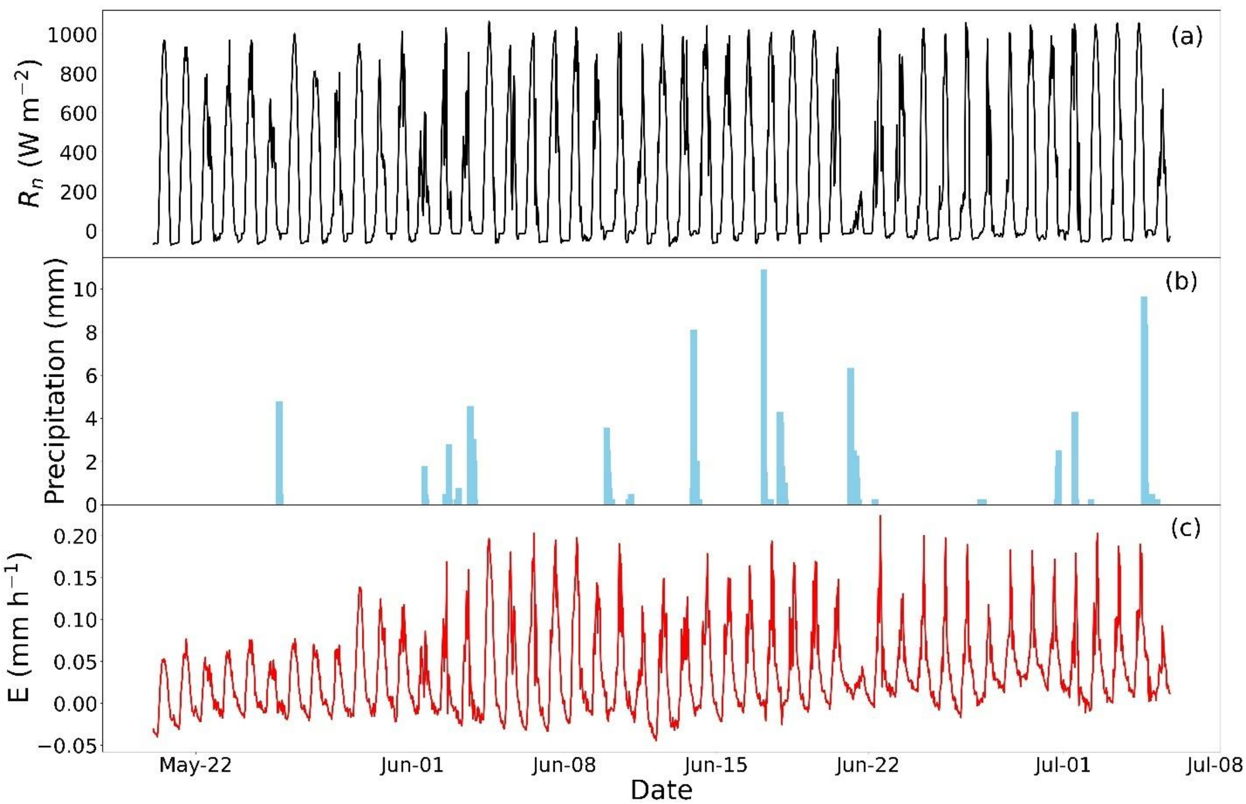

Figure 3-7 (a) Net radiation, (b) precipitation and (c) total soil evaporation from 9-63 mm soil layer measured at the Gypsum site.

Chapter 4 - General Conclusion

Soil evaporation plays a substantial role in the water balances of arid regions. However, it is arguably one of the most challenging hydrological processes to estimate and measure accurately. Although several approaches to estimate soil evaporation exist, their potential to capture the highly dynamic near-surface soil water and heat processes involved in soil water evaporation is limited. Given the practical difficulties and uncertainties of the existing approaches, a measurement-based soil sensible heat balance has been developed to determine in situ soil water evaporation dynamics utilizing heat pulse probes. This thesis aimed to deepen our understanding of the complex temporal and spatial patterns of heat transfer and evaporation within soil under field conditions.

The first chapter focused on constructing and calibrating three-needle heat pulse probes for understanding the influence of soil moisture on near-surface soil thermal properties and how these properties change with depth. It also aimed at evaluating TNHP probes for capturing the dynamics of soil sensible heat flux and storage at various soil depths during consecutive wetting-drying cycles. The results revealed that the temperature offsets reduced discrepancies in temperature readings by the thermistors of the same probe. The apparent probe spacing values determined from laboratory calibration were close to the physical probe spacing. The results also showed that soil moisture had an influential role in increasing soil thermal conductivity (λ), and volumetric heat capacity (C), with larger impact on C because of its linear relationship with soil water content. Furthermore, the study highlighted that soil temperature gradient was the driving force for soil sensible heat flux, and heat flux had decreasing magnitude as well as amplitude with depth. Also, soil sensible heat storage decreased with depth with greater diurnal fluctuations near the surface.

In the second chapter, our objective was to quantify near-surface soil evaporation using a measurement-based sensible heat balance approach in the inter-rows of corn plants and in bare soil. This study also focused on comparing the evaporation estimates from the SHB approach to independent estimates of evaporation from energy balance (Eddy Covariance) and mass balance microlysimeter) methods. The comparison of SHB estimated evaporation to the evaporation estimates from the eddy covariance method revealed that EC method recorded higher evaporation values. A regression analysis indicated a fairly good correlation between the two methods with $R^2 = 0.62$ and root-mean-square-error (RMSE) of 0.039 mmh^{-1} for 10 days of measurement. Despite the scale difference in the two methods, the results indicate the potential of the heat balance method. Reducing the undetectable zone using an improved probe design with closer spacing, could accurately capture sub-surface evaporation, and consequently reduce the gap in the evaporation estimate. Contrary to our expectation of higher correlation between evaporation estimates from the SHB and microlysimeter methods, larger discrepancy in measurements were observed. This was likely due to the combined effect of the inability of the HPP probes to measure Stage 1 evaporation, and the restricted capillary flow of water in the microlysimeter. The time-series and depth wise variation of sub-surface evaporation indicated that most of the total evaporation was contributed by shallower soil layers, and there was significant time lag in daily peaks from the deeper layers.

Overall, this study findings suggest good potential for using SHB method to determine soil evaporation under drying-wetting cycles. Modifications to the SHB technique to allow evaporation estimation when evaporation front stays at the surface, could improve the range of measurement conditions. Furthermore, combining this technique with other approaches of ET partitioning could help in modifying the existing soil evaporation models for better accuracy.

References

Abu-Hamdeh, N. H. (2003). Thermal Properties of Soils as affected by Density and Water Content. *Biosystems Engineering*, *86*(1), 97–102. https://doi.org/10.1016/S1537-5110(03)00112-0

Austin, A. T., Yahdjian, L., Stark, J. M., Belnap, J., Porporato, A., Norton, U., Ravetta, D. A., & Schaeffer, S. M. (2004). Water pulses and biogeochemical cycles in arid and semiarid ecosystems. *Oecologia*, *141*(2), 221–235. https://doi.org/10.1007/s00442-004-1519-1

Baldocchi, D. D. (2020). How eddy covariance flux measurements have contributed to our understanding of Global Change Biology. *Global Change Biology*, *26*(1), 242–260. https://doi.org/10.1111/gcb.14807

Bastiaanssen, W. G. M., Karimi, P., Rebelo, L.-M., Duan, Z., Senay, G., Muthuwatte, L., & Smakhtin, V. (2014). Earth Observation Based Assessment of the Water Production and Water Consumption of Nile Basin Agro-Ecosystems. *Remote Sensing*, *6*(11), Article 11. https://doi.org/10.3390/rs61110306

Berg, A., & Sheffield, J. (2019). *Evapotranspiration Partitioning in CMIP5 Models: Uncertainties and Future Projections*. https://doi.org/10.1175/JCLI-D-18-0583.1

Boast, C. W., & Robertson, T. M. (1982). A “Micro-Lysimeter” Method for Determining Evaporation from Bare Soil: Description and Laboratory Evaluation. *Soil Science Society of America Journal*, *46*(4), 689–696. https://doi.org/10.2136/sssaj1982.03615995004600040005x

Böhm, W., Maduakor, H., & Taylor, H. M. (1977). Comparison of Five Methods for Characterizing Soybean Rooting Density and Development. *Agronomy Journal*, *69*(3), 415–419. https://doi.org/10.2134/agronj1977.00021962006900030021x

Bristow, K. L., Kluitenberg, G. J., & Horton, R. (1994). Measurement of Soil Thermal Properties with a Dual-Probe Heat-Pulse Technique. *Soil Science Society of America Journal*, *58*(5), 1288–1294. https://doi.org/10.2136/sssaj1994.03615995005800050002x

Campbell, G. S., Calissendorff, C., & Williams, J. H. (1991). Probe for Measuring Soil Specific Heat Using A Heat-Pulse Method. *Soil Science Society of America Journal*, *55*(1), 291–293. https://doi.org/10.2136/sssaj1991.03615995005500010052x

Cobos, D. R., & Baker, J. M. (2003). In Situ Measurement of Soil Heat Flux with the Gradient Method. *Vadose Zone Journal*, *2*(4), 589–594. https://doi.org/10.2136/vzj2003.5890

Da Rocha, A. E. Q., Santos, E. A., & Patrignani, A. (2022). Partitioning evapotranspiration in a tallgrass prairie using micrometeorological and water use efficiency approaches under contrasting rainfall regimes. *Journal of Hydrology*, *608*, 127624. https://doi.org/10.1016/j.jhydrol.2022.127624

Deol, P., Heitman, J., Amoozegar, A., Ren, T., & Horton, R. (2012). Quantifying nonisothermal subsurface soil water evaporation. *Water Resources Research*, *48*(11). https://doi.org/10.1029/2012WR012516

Deol, P. K., Heitman, J. L., Amoozegar, A., Ren, T., & Horton, R. (2014). Inception and Magnitude of Subsurface Evaporation for a Bare Soil with Natural Surface Boundary Conditions. *Soil Science Society of America Journal*, *78*(5), 1544–1551. https://doi.org/10.2136/sssaj2013.12.0520

Evett, S. R., Warrick, A. W., & Matthias, A. D. (1995). Wall Material and Capping Effects on Microlysimeter Temperatures and Evaporation. *Soil Science Society of America Journal*, *59*(2), 329–336. https://doi.org/10.2136/sssaj1995.03615995005900020009x

Fisher, J. B., Melton, F., Middleton, E., Hain, C., Anderson, M., Allen, R., McCabe, M. F., Hook, S., Baldocchi, D., Townsend, P. A., Kilic, A., Tu, K., Miralles, D. D., Perret, J., Lagouarde, J.-P., Waliser, D., Purdy, A. J., French, A., Schimel, D., … Wood, E. F. (2017). The future of evapotranspiration: Global requirements for ecosystem functioning, carbon and climate feedbacks, agricultural management, and water resources. *Water Resources Research*, *53*(4), 2618–2626. https://doi.org/10.1002/2016WR020175

Forsythe, W. E. (1954). Smithsonian physical tables. *Smithsonian miscellaneous collections*.

Fritschen, L. J., & Fritschen, C. L. (2005). Bowen Ratio Energy Balance Method. In *Micrometeorology in Agricultural Systems* (pp. 397–405). John Wiley & Sons, Ltd. https://doi.org/10.2134/agronmonogr47.c17

Fuchs, M., & Tanner, C. B. (1968). Calibration and Field Test of Soil Heat Flux Plates. *Soil Science Society of America Journal*, *32*(3), 326–328. https://doi.org/10.2136/sssaj1968.03615995003200030021x

Gao, Z., Russell, E. S., Missik, J. E. C., Huang, M., Chen, X., Strickland, C. E., Clayton, R., Arntzen, E., Ma, Y., & Liu, H. (2017). A novel approach to evaluate soil heat flux calculation: An analytical review of nine methods. *Journal of Geophysical Research: Atmospheres*, *122*(13), 6934–6949. https://doi.org/10.1002/2017JD027160

Gardner, H. R., & Hanks, R. J. (1966). Evaluation of the Evaporation Zone in Soil by Measurement of Heat Flux. *Soil Science Society of America Journal*, *30*(4), 425–428. https://doi.org/10.2136/sssaj1966.03615995003000040010x

Gavlak, R., Horneck, D., & Miller, R. O. (2005). Particle size analysis: Hydrometer method. *Soil, plant and water reference methods for the western region*, *128130*.

Gong, C., Wang, W., Zhang, Z., Wang, H., Luo, J., & Brunner, P. (2020). Comparison of field methods for estimating evaporation from bare soil using lysimeters in a semi-arid area. *Journal of Hydrology*, *590*, 125334. https://doi.org/10.1016/j.jhydrol.2020.125334

Good, S. P., Noone, D., & Bowen, G. (2015). Hydrologic connectivity constrains partitioning of global terrestrial water fluxes. *Science*, *349*(6244), 175–177. https://doi.org/10.1126/science.aaa5931

Ham, J. M., & Benson, E. J. (2004). On the Construction and Calibration of Dual-Probe Heat Capacity Sensors. *Soil Science Society of America Journal*, *68*(4), 1185–1190. https://doi.org/10.2136/sssaj2004.1185

Han, J., Lin, J., & Dai, Y. (2017). Numerical Modeling of Soil Evaporation Process and Its Stages Dividing during a Drying Cycle. *Geofluids*, *2017*(1), 5892867. https://doi.org/10.1155/2017/5892867

Hanks, R. J., & Jacobs, H. S. (1971). Comparison of the Calorimetric and Flux Meter Measurements of Soil Heat Flow. *Soil Science Society of America Journal*, *35*(5), 671–674. https://doi.org/10.2136/sssaj1971.03615995003500050017x

Heitman, J. L., Basinger, J. M., Kluitenberg, G. J., Ham, J. M., Frank, J. M., & Barnes, P. L. (2003). Field Evaluation of the Dual-Probe Heat-Pulse Method for Measuring Soil Water Content. *Vadose Zone Journal*, *2*(4), 552–560. https://doi.org/10.2136/vzj2003.5520

Heitman, J. L., Horton, R., Sauer, T. J., & DeSutter, T. M. (2008a). *Sensible Heat Observations Reveal Soil-Water Evaporation Dynamics*. https://doi.org/10.1175/2007JHM963.1

Heitman, J. L., Horton, R., Sauer, T. J., Ren, T. S., & Xiao, X. (2010). Latent heat in soil heat flux measurements. *Agricultural and Forest Meteorology*, *150*(7–8), 1147–1153. https://doi.org/10.1016/j.agrformet.2010.04.017

Heitman, J. L., Xiao, X., Horton, R., & Sauer, T. J. (2008b). Sensible heat measurements indicating depth and magnitude of subsurface soil water evaporation. *Water Resources Research*, *44*(4), 2008WR006961. https://doi.org/10.1029/2008WR006961

Heitman, J. l., Zhang, X., Xiao, X., Ren, T., & Horton, R. (2020). Advances in heat-pulse methods: Measuring soil water evaporation with sensible heat balance. *Soil Science Society of America Journal*, *84*(5), 1371–1375. https://doi.org/10.1002/saj2.20149

Heusinkveld, B. G., Jacobs, A. F. G., Holtslag, A. A. M., & Berkowicz, S. M. (2004). Surface energy balance closure in an arid region: Role of soil heat flux. *Agricultural and Forest Meteorology*, *122*(1–2), 21–37. https://doi.org/10.1016/j.agrformet.2003.09.005

Hopmans, J. W., Šimunek, J., & Bristow, K. L. (2002). Indirect estimation of soil thermal properties and water flux using heat pulse probe measurements: Geometry and dispersion effects. *Water Resources Research*, *38*(1), 7-1-7–14. https://doi.org/10.1029/2000WR000071

Irmak, S., & Kukal, M. S. (2022). Evapotranspiration, Transpiration, and Evaporation Processes and Modeling in the Soil–Residue–Canopy System. In *Modeling Processes and Their Interactions in Cropping Systems* (pp. 53–114). John Wiley & Sons, Ltd. https://doi.org/10.1002/9780891183860.ch3

Jacobs, A. F. G., Heusinkveld, B. G., & Holtslag, A. A. M. (2011). Long-term record and analysis of soil temperatures and soil heat fluxes in a grassland area, The Netherlands. *Agricultural and Forest Meteorology*, *151*(7), 774–780. https://doi.org/10.1016/j.agrformet.2011.01.002

Kamai, T., Kluitenberg, G. J., & Hopmans, J. W. (2015). A Dual-Probe Heat-Pulse Sensor with Rigid Probes for Improved Soil Water Content Measurement. *Soil Science Society of America Journal*, *79*(4), 1059–1072. https://doi.org/10.2136/sssaj2015.01.0025

Katul, G. G., Oren, R., Manzoni, S., Higgins, C., & Parlange, M. B. (2012). Evapotranspiration: A process driving mass transport and energy exchange in the soil-plant-atmosphere-climate system. *Reviews of Geophysics*, *50*(3). https://doi.org/10.1029/2011RG000366

Knight, J. H., & Kluitenberg, G. J. (2004). Simplified Computational Approach for Dual-Probe Heat-Pulse Method. *Soil Science Society of America Journal*, *68*(2), 447–449. https://doi.org/10.2136/sssaj2004.4470

Knight, J. H., Kluitenberg, G. J., Kamai, T., & Hopmans, J. W. (2012). Semianalytical Solution for Dual-Probe Heat-Pulse Applications that Accounts for Probe Radius and Heat Capacity. *Vadose Zone Journal*, *11*(2), vzj2011.0112. https://doi.org/10.2136/vzj2011.0112

Kojima, Y., Heitman, J. L., Flerchinger, G. N., Ren, T., & Horton, R. (2016). Sensible Heat Balance Estimates of Transient Soil Ice Contents. *Vadose Zone Journal*, *15*(5), vzj2015.10.0134. https://doi.org/10.2136/vzj2015.10.0134

Kool, D., Agam, N., Lazarovitch, N., Heitman, J. L., Sauer, T. J., & Ben-Gal, A. (2014). A review of approaches for evapotranspiration partitioning. *Agricultural and Forest Meteorology*, *184*, 56–70. https://doi.org/10.1016/j.agrformet.2013.09.003

Kool, D., Heitman, J. L., Lazarovitch, N., Agam, N., Sauer, T. J., & Ben-Gal, A. (2016). In Situ Thermistor Calibration for Improved Measurement of Soil Temperature Gradients. *Soil Science Society of America Journal*, *80*(6), 1514–1519. https://doi.org/10.2136/sssaj2016.05.0134

Kustas, W. P., Prueger, J. H., Hatfield, J. L., Ramalingam, K., & Hipps, L. E. (2000). Variability in soil heat flux from a mesquite dune site. *Agricultural and Forest Meteorology*, *103*(3), 249–264. https://doi.org/10.1016/S0168-1923(00)00131-3

Lawrence, D. M., Thornton, P. E., Oleson, K. W., & Bonan, G. B. (2007). *The Partitioning of Evapotranspiration into Transpiration, Soil Evaporation, and Canopy Evaporation in a GCM: Impacts on Land–Atmosphere Interaction*. https://doi.org/10.1175/JHM596.1

Leuning, R., Van Gorsel, E., Massman, W. J., & Isaac, P. R. (2012). Reflections on the surface energy imbalance problem. *Agricultural and Forest Meteorology*, *156*, 65–74. https://doi.org/10.1016/j.agrformet.2011.12.002

Li, X., Gentine, P., Lin, C., Zhou, S., Sun, Z., Zheng, Y., Liu, J., & Zheng, C. (2019). A simple and objective method to partition evapotranspiration into transpiration and evaporation at eddy-covariance sites. *Agricultural and Forest Meteorology*, *265*, 171–182. https://doi.org/10.1016/j.agrformet.2018.11.017

Licht, M., Archontoulis, S., & Hatfield, J. L. (2017). Corn water use and evapotranspiration. *Iowa State University Extension and Outreach*.

Liu, G., Lu, Y., Wen, M., Ren, T., & Horton, R. (2020). Advances in the heat-pulse technique: Improvements in measuring soil thermal properties. *Soil Science Society of America Journal*, *84*(5), 1361–1370. https://doi.org/10.1002/saj2.20148

Lu, S., Ma, C., Meng, P., Zhang, J., Zhang, X., Lu, Y., & Yin, C. (2016). Experimental investigation of subsurface soil water evaporation on soil heat flux plate measurement. *Applied Thermal Engineering*, *93*, 433–437. https://doi.org/10.1016/j.applthermaleng.2015.09.058

Lu, S., Wang, H., Meng, P., Zhang, J., & Zhang, X. (2018). Determination of soil ground heat flux through heat pulse and plate methods: Effects of subsurface latent heat on surface energy balance closure. *Agricultural and Forest Meteorology*, *260–261*, 176–182. https://doi.org/10.1016/j.agrformet.2018.06.008

Lu, Y., Wang, Y., & Ren, T. (2013). Using Late Time Data Improves the Heat-Pulse Method for Estimating Soil Thermal Properties with the Pulsed Infinite Line Source Theory. *Vadose Zone Journal*, *12*(4), vzj2013.01.0011. https://doi.org/10.2136/vzj2013.01.0011

Massman, W. J. (1993). Errors Associated with the Combination Method for Estimating Soil Heat Flux. *Soil Science Society of America Journal*, *57*(5), 1198–1202. https://doi.org/10.2136/sssaj1993.03615995005700050006x

Mellouli, H. J., van Wesemael, B., Poesen, J., & Hartmann, R. (2000). Evaporation losses from bare soils as influenced by cultivation techniques in semi-arid regions. *Agricultural Water Management*, *42*(3), 355–369. https://doi.org/10.1016/S0378-3774(99)00040-2

Meng, F., Li, T., Sheng, W., Dixon, C., Zhou, R., & Jones, S. B. (2023). Heat pulse probe design optimization using numerical simulation. *Geoderma*, *436*, 116534. https://doi.org/10.1016/j.geoderma.2023.116534

Merlin, O., Stefan, V. G., Amazirh, A., Chanzy, A., Ceschia, E., Er-Raki, S., Gentine, P., Tallec, T., Ezzahar, J., Bircher, S., Beringer, J., & Khabba, S. (2016). Modeling soil evaporation efficiency in a range of soil and atmospheric conditions using a meta-analysis approach. *Water Resources Research*, *52*(5), 3663–3684. https://doi.org/10.1002/2015WR018233

Meyers, T. P., & Baldocchi, D. D. (2005). Current Micrometeorological Flux Methodologies with Applications in Agriculture. In *Micrometeorology in Agricultural Systems* (pp. 381–396). John Wiley & Sons, Ltd. https://doi.org/10.2134/agronmonogr47.c16

Naruke, C., Sheng, W., Zhou, R., & Jones, S. B. (2021). Standardizing Heat Pulse Probe measurements for thermal property determination using ice and water. *Agricultural and Forest Meteorology*, *308–309*, 108610. https://doi.org/10.1016/j.agrformet.2021.108610

Newman, B. D., Wilcox, B. P., Archer, S. R., Breshears, D. D., Dahm, C. N., Duffy, C. J., McDowell, N. G., Phillips, F. M., Scanlon, B. R., & Vivoni, E. R. (2006). Ecohydrology of water-limited environments: A scientific vision. *Water Resources Research*, *42*(6). https://doi.org/10.1029/2005WR004141

Newville, M., Stensitzki, T., Allen, D. B., & Ingargiola, A. (2014). *LMFIT: Non-Linear Least-Square Minimization and Curve-Fitting for Python* (Version 0.8.0) [Computer software]. Zenodo. https://doi.org/10.5281/zenodo.11813

Ochsner, T. E., Horton, R., & Ren, T. (2001). A New Perspective on Soil Thermal Properties. *Soil Science Society of America Journal*, *65*(6), 1641–1647. https://doi.org/10.2136/sssaj2001.1641

Ochsner, T. E., Horton, R., & Ren, T. (2003). Use of the Dual-Probe Heat-Pulse Technique to Monitor Soil Water Content in the Vadose Zone. *Vadose Zone Journal*, *2*(4), 572–579. https://doi.org/10.2136/vzj2003.5720

Ochsner, T. E., Sauer, T. J., & Horton, R. (2006). Field Tests of the Soil Heat Flux Plate Method and Some Alternatives. *Agronomy Journal*, *98*(4), 1005–1014. https://doi.org/10.2134/agronj2005.0249

Ochsner, T. E., Sauer, T. J., & Horton, R. (2007). Soil Heat Storage Measurements in Energy Balance Studies. *Agronomy Journal*, *99*(1), 311–319. https://doi.org/10.2134/agronj2005.0103S

Or, D., Lehmann, P., Shahraeeni, E., & Shokri, N. (2013). Advances in Soil Evaporation Physics—A Review. *Vadose Zone Journal*, *12*(4), vzj2012.0163. https://doi.org/10.2136/vzj2012.0163

Peng, W., Lu, Y., Ren, T., & Horton, R. (2021). Application of infinite line source and cylindrical-perfect-conductors theories to heat pulse measurements with large sensors. *Soil Science Society of America Journal*, *85*(4), 1050–1059. https://doi.org/10.1002/saj2.20250

Peng, X., Wang, Y., Heitman, J., Ochsner, T., Horton, R., & Ren, T. (2017). Measurement of soil-surface heat flux with a multi-needle heat-pulse probe. *European Journal of Soil Science*, *68*(3), 336–344. https://doi.org/10.1111/ejss.12421

Qiu, G. Y., & Ben-Asher, J. (2010). Experimental Determination of Soil Evaporation Stages with Soil Surface Temperature. *Soil Science Society of America Journal*, *74*(1), 13–22. https://doi.org/10.2136/sssaj2008.0135

Ren, T., Kluitenberg, G. J., & Horton, R. (2000). Determining Soil Water Flux and Pore Water Velocity by a Heat Pulse Technique. *Soil Science Society of America Journal*, *64*(2), 552–560. https://doi.org/10.2136/sssaj2000.642552x

Rumana, K. (2015). *Novel Techniques to Determine Soil Evaporation Rates: Heat Pulse Probe and Automated Microlysimeter*.

Sakai, M., Jones, S. B., & Tuller, M. (2011). Numerical evaluation of subsurface soil water evaporation derived from sensible heat balance. *Water Resources Research*, *47*(2). https://doi.org/10.1029/2010WR009866

Sauer, T. J., & Horton, R. (2005). Soil Heat Flux. In *Micrometeorology in Agricultural Systems* (pp. 131–154). John Wiley & Sons, Ltd. https://doi.org/10.2134/agronmonogr47.c7

Scott, R. L., & Biederman, J. A. (2017). Partitioning evapotranspiration using long-term carbon dioxide and water vapor fluxes. *Geophysical Research Letters*, *44*(13), 6833–6840. https://doi.org/10.1002/2017GL074324

Song, Y., Kirkham, M. B., Ham, J. M., & Kluitenberg, G. J. (1999). Dual probe heat pulse technique for measuring soil water content and sunflower water uptake. *Soil and Tillage Research*, *50*(3), 345–348. https://doi.org/10.1016/S0167-1987(99)00014-8

Song, Y., Kirkham, M. B., Ham, J. M., & Kluitenberg, G. J. (2000). Root-zone hydraulic lift evaluated with the dual-probe heat-pulse technique. *Soil Research*, *38*(5), 927–935. https://doi.org/10.1071/sr99096

Stehfest, H. (1970a). Algorithm 368: Numerical inversion of Laplace transforms [D5]. *Communications of the ACM*, *13*(1), 47–49. https://doi.org/10.1145/361953.361969

Stehfest, H. (1970b). Remark on algorithm 368: Numerical inversion of Laplace transforms. *Communications of the ACM*, *13*(10), 624. https://doi.org/10.1145/355598.362787

Suleiman, A. A., & Ritchie, J. T. (2003). Modeling Soil Water Redistribution during Second-Stage Evaporation. *Soil Science Society of America Journal*, *67*(2), 377–386. https://doi.org/10.2136/sssaj2003.3770

Tarara, J. M., & Ham, J. M. (1997). Measuring Soil Water Content in the Laboratory and Field with Dual-Probe Heat-Capacity Sensors. *Agronomy Journal*, *89*(4), 535–542. https://doi.org/10.2134/agronj1997.00021962008900040001x

Trautz, A. C., Smits, K. M., Schulte, P., & Illangasekare, T. H. (2014). Sensible Heat Balance and Heat-Pulse Method Applicability to In Situ Soil-Water Evaporation. *Vadose Zone Journal*, *13*(1), vzj2012.0215. https://doi.org/10.2136/vzj2012.0215

Valente, A., Saraiva, A. A., Ferreira, N. M. F., & Soares, S. (2018). *On the Design, Construction and Calibration of Dual-Probe Heat-Pulse Soil Moisture Sensor: Towards an Industrial Solution*.

Wagle, P., Skaggs, T. H., Gowda, P. H., Northup, B. K., & Neel, J. P. S. (2020). Flux variance similarity-based partitioning of evapotranspiration over a rainfed alfalfa field using high frequency eddy covariance data. *Agricultural and Forest Meteorology*, *285–286*, 107907. https://doi.org/10.1016/j.agrformet.2020.107907

Wang, D., & Wang, L. (2017). Dynamics of evapotranspiration partitioning for apple trees of different ages in a semiarid region of northwest China. *Agricultural Water Management*, *191*, 1–15. https://doi.org/10.1016/j.agwat.2017.05.010

Wang, P., Yamanaka, T., Li, X.-Y., & Wei, Z. (2015). Partitioning evapotranspiration in a temperate grassland ecosystem: Numerical modeling with isotopic tracers. *Agricultural and Forest Meteorology*, *208*, 16–31. https://doi.org/10.1016/j.agrformet.2015.04.006

Wang, W., Smith, J. A., Ramamurthy, P., Baeck, M. L., Bou-Zeid, E., & Scanlon, T. M. (2016). On the correlation of water vapor and CO2: Application to flux partitioning of evapotranspiration. *Water Resources Research*, *52*(12), 9452–9469. https://doi.org/10.1002/2015WR018161

Wang, Y., Horton, R., Xue, X., & Ren, T. (2021). Partitioning evapotranspiration by measuring soil water evaporation with heat-pulse sensors and plant transpiration with sap flow gauges. *Agricultural Water Management*, *252*, 106883. https://doi.org/10.1016/j.agwat.2021.106883

Wang, Y., Ochsner, T., Heitman, J., Horton, R., Xue, X., & Ren, T. (2017). Weighing Lysimeter Data Confirm the Accuracy and Precision of the Heat-Pulse Technique for Measuring

Daily Soil Evaporation. *Soil Science Society of America Journal*, *81*(5), 1074–1078. https://doi.org/10.2136/sssaj2017.02.0049n

Waring, R. H., & Running, S. W. (2010). *Forest Ecosystems: Analysis at Multiple Scales*. Elsevier.

Wilcox, B., Breshears, D., & Seyfried, M. (2003). Rangelands, Water Balance on. *Encyclopedia of Water Science*.

Williams, D. G., Cable, W., Hultine, K., Hoedjes, J. C. B., Yepez, E. A., Simonneaux, V., Er-Raki, S., Boulet, G., De Bruin, H. A. R., Chehbouni, A., Hartogensis, O. K., & Timouk, F. (2004). Evapotranspiration components determined by stable isotope, sap flow and eddy covariance techniques. *Agricultural and Forest Meteorology*, *125*(3–4), 241–258. https://doi.org/10.1016/j.agrformet.2004.04.008

Wutzler, T., Lucas-Moffat, A., Migliavacca, M., Knauer, J., Sickel, K., Šigut, L., Menzer, O., & Reichstein, M. (2018). *Basic and extensible post-processing of eddy covariance flux data with REddyProc*. https://doi.org/10.5194/bg-2018-56

Xiao, X., Heitman, J. l., Sauer, T. j., Ren, T., & Horton, R. (2014). Sensible Heat Balance Measurements of Soil Water Evaporation beneath a Maize Canopy. *Soil Science Society of America Journal*, *78*(2), 361–368. https://doi.org/10.2136/sssaj2013.08.0371

Xiao, X., Horton, R., Sauer, T. J., Heitman, J. L., & Ren, T. (2011). Cumulative Soil Water Evaporation as a Function of Depth and Time. *Vadose Zone Journal*, *10*(3), 1016–1022. https://doi.org/10.2136/vzj2010.0070

Xiao, X., Sauer, T., Singer, J. W., Horton, R., Ren, T., & Heitman, J. (2016). Partitioning Evaporation and Transpiration in a Maize Field Using Heat-Pulse Sensors for Evaporation Measurement. *Transactions of the ASABE, 59,* 591–599. https://doi.org/10.13031/trans.59.11059

Xiao, Z., Lu, S., Heitman, J., Horton, R., & Ren, T. (2012). Measuring Subsurface Soil-Water Evaporation with an Improved Heat-Pulse Probe. *Soil Science Society of America Journal*, *76*(3), 876–879. https://doi.org/10.2136/sssaj2011.0052n

Yu, L., Zhou, S., Zhao, X., Gao, X., Jiang, K., Zhang, B., Cheng, L., Song, X., & Siddique, K. H. M. (2022). Evapotranspiration Partitioning Based on Leaf and Ecosystem Water Use Efficiency. *Water Resources Research*, *58*(9), e2021WR030629. https://doi.org/10.1029/2021WR030629

Zeggaf, A. T., Takeuchi, S., Dehghanisanij, H., Anyoji, H., & Yano, T. (2008). A Bowen Ratio Technique for Partitioning Energy Fluxes between Maize Transpiration and Soil Surface Evaporation. *Agronomy Journal*, *100*(4), 988–996. https://doi.org/10.2134/agronj2007.0201

Zhang, K., Ma, J., Zhu, G., Ma, T., Han, T., & Feng, L. L. (2017). Parameter sensitivity analysis and optimization for a satellite-based evapotranspiration model across multiple sites using Moderate Resolution Imaging Spectroradiometer and flux data. *Journal of Geophysical Research: Atmospheres, 122*(1), 230–245. https://doi.org/10.1002/2016JD025768

Zhang, K., Zhu, G., Ma, J., Yang, Y., Shang, S., & Gu, C. (2019). Parameter Analysis and Estimates for the MODIS Evapotranspiration Algorithm and Multiscale Verification. *Water Resources Research*, *55*(3), 2211–2231. https://doi.org/10.1029/2018WR023485

Zhang, M., Lu, Y., Ren, T., & Horton, R. (2020). In-situ probe spacing calibration improves the heat pulse method for measuring soil heat capacity and water content. *Soil Science Society of America Journal*, *84*(5), 1620–1629. https://doi.org/10.1002/saj2.20124

Zhang, S., Wen, X., Wang, J., Yu, G., & Sun, X. (2010). The use of stable isotopes to partition evapotranspiration fluxes into evaporation and transpiration. *Acta Ecologica Sinica*, *30*(4), 201–209. https://doi.org/10.1016/j.chnaes.2010.06.003

Zhang, X., Heitman, J., Horton, R., & Ren, T. (2014). Measuring Near-Surface Soil Thermal Properties with the Heat-Pulse Method: Correction of Ambient Temperature and Soil–Air Interface Effects. *Soil Science Society of America Journal*, *78*(5), 1575–1583. https://doi.org/10.2136/sssaj2014.01.0014

Zhou, S., Yu, B., Zhang, Y., Huang, Y., & Wang, G. (2016). Partitioning evapotranspiration based on the concept of underlying water use efficiency. *Water Resources Research*, *52*(2), 1160–1175. https://doi.org/10.1002/2015WR017766

Appendix A - Heat flux and evaporation measurement

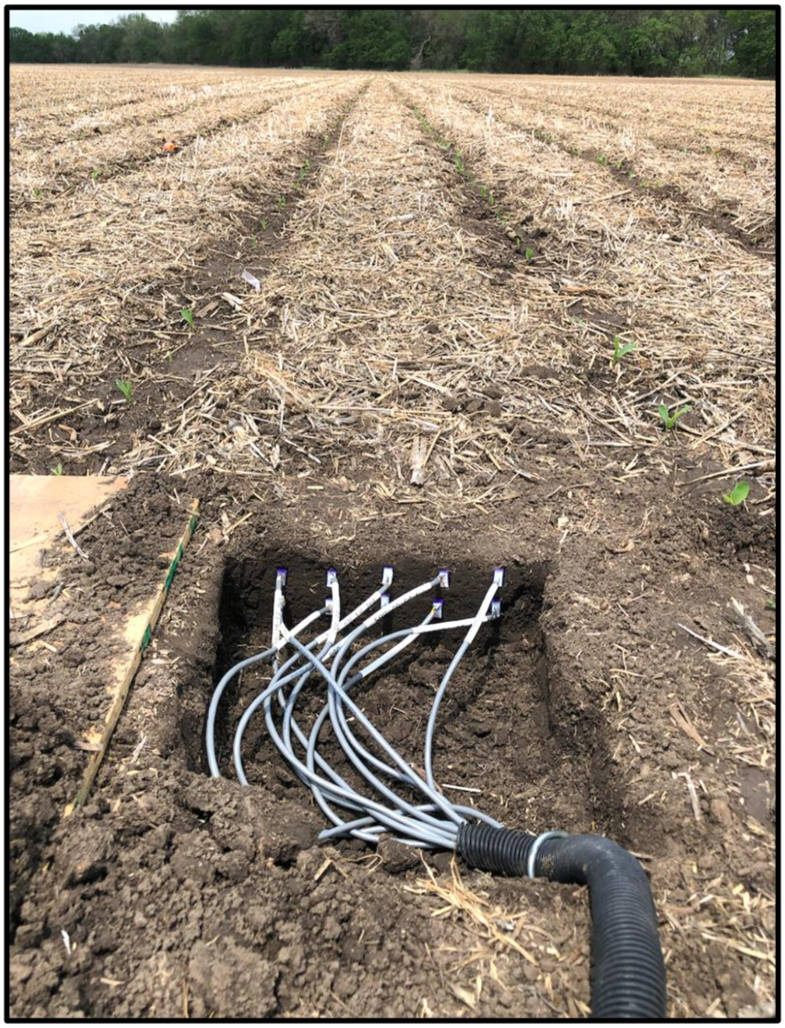

Appendix Figure A-1 HP probe installation in the inter-rows of corn.